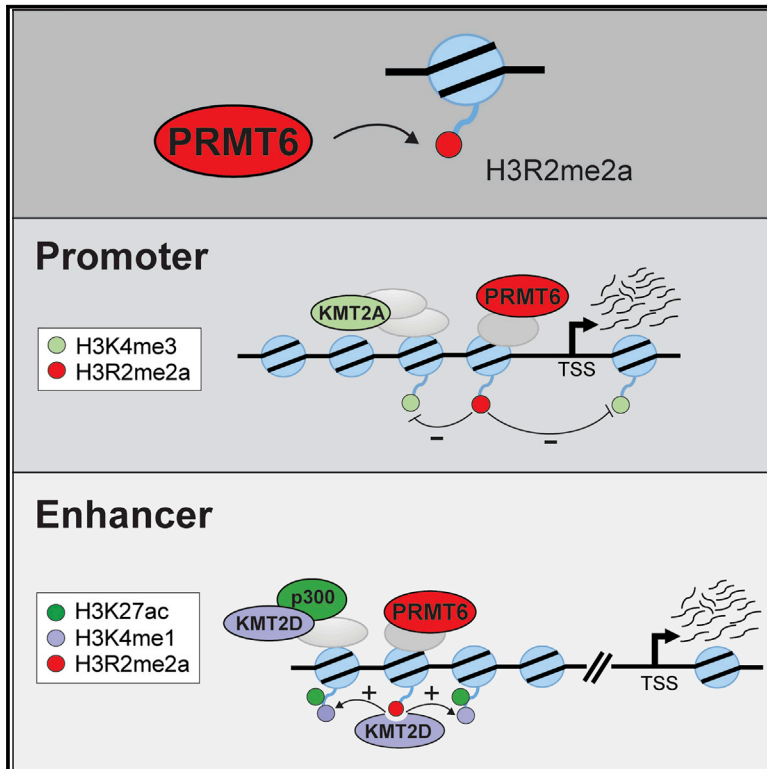


# Cell Reports

## Genomic Location of PRMT6-Dependent H3R2 Methylation Is Linked to the Transcriptional Outcome of Associated Genes

### Graphical Abstract



### Authors

Caroline Bouchard, Peeyush Sahu, Marion Meixner, ..., Thorsten Stiewe, Sjaak Philipsen, Uta-Maria Bauer

### Correspondence

bauer@imt.uni-marburg.de

### In Brief

Bouchard et al. identify the genome-wide, PRMT6-dependent occurrence of H3R2me2a in a cell model of neural differentiation. H3R2me2a is localized at promoters and enhancers of active genes and influences the chromatin recruitment of histone lysine methyltransferases. Thereby, H3R2me2a modulates the deposition of adjacent histone H3 marks and regulates the transcriptional output of genes relevant for pluripotency and differentiation.

### Highlights

- PRMT6 deposits H3R2me2a at promoters as well as enhancers of active genes
- H3R2me2a influences the occurrence of adjacent histone marks (H3K4me3, H3K4me1, H3K27ac)
- H3R2me2a contributes to gene repression at promoters and gene activation at enhancers
- PRMT6/H3R2me2a modulate the transcription of important neural differentiation genes

### Data and Software Availability

GSE107612



# Genomic Location of PRMT6-Dependent H3R2 Methylation Is Linked to the Transcriptional Outcome of Associated Genes

Caroline Bouchard,<sup>1,12</sup> Peeyush Sahu,<sup>1,12</sup> Marion Meixner,<sup>1,12</sup> René Reiner Nötzold,<sup>1,12</sup> Marco B. Rust,<sup>2</sup> Elisabeth Kremmer,<sup>3</sup> Regina Feederle,<sup>4</sup> Gene Hart-Smith,<sup>5</sup> Florian Finkernagel,<sup>6</sup> Marek Bartkuhn,<sup>7</sup> Soni Savai Pullamsetti,<sup>8</sup> Andrea Nist,<sup>9</sup> Thorsten Stiewe,<sup>9,10</sup> Sjaak Philipsen,<sup>11</sup> and Uta-Maria Bauer<sup>1,13,\*</sup>

<sup>1</sup>Institute for Molecular Biology and Tumor Research (IMT), Philipps-University Marburg, Hans-Meerwein-Strasse 2, BMFZ, 35043 Marburg, Germany

<sup>2</sup>Molecular Neurobiology Group, Institute of Physiological Chemistry, Philipps-University Marburg, Karl-von-Frisch-Strasse 1, 35043 Marburg, Germany

<sup>3</sup>Institute of Molecular Immunology, Helmholtz Zentrum München, German Research Center for Environmental Health GmbH, 81377 Munich, Germany

<sup>4</sup>Monoclonal Antibody Core Facility, Institute for Diabetes and Obesity, Helmholtz Zentrum München, German Research Center for Environmental Health GmbH, Ingolstädter Landstrasse 1, 85764 Neuherberg, Germany

<sup>5</sup>School of Biotechnology and Biomolecular Sciences, University of New South Wales, Sydney, New South Wales 2052, Australia

<sup>6</sup>Center for Tumor Biology and Immunology (ZTI), Philipps-University Marburg, Hans-Meerwein-Strasse 3, 35043 Marburg, Germany

<sup>7</sup>Institute for Genetics, Justus-Liebig-University Giessen, Heinrich-Buff-Ring 58-62, 35392 Giessen, Germany

<sup>8</sup>Department of Lung Development and Remodeling, Max-Planck-Institute for Heart and Lung Research, Member of the German Center for Lung Research (DZL), Bad Nauheim, Germany

<sup>9</sup>Genomics Core Facility, Philipps-University Marburg, Hans-Meerwein-Strasse 3, 35043 Marburg, Germany

<sup>10</sup>Institute of Molecular Oncology, Philipps-University Marburg, Hans-Meerwein-Strasse 3, 35043 Marburg, Germany

<sup>11</sup>Department of Cell Biology, Erasmus MC, Rotterdam, the Netherlands

<sup>12</sup>These authors contributed equally

<sup>13</sup>Lead Contact

\*Correspondence: [bauer@imt.uni-marburg.de](mailto:bauer@imt.uni-marburg.de)  
<https://doi.org/10.1016/j.celrep.2018.08.052>

## SUMMARY

Protein arginine methyltransferase 6 (PRMT6) catalyzes asymmetric dimethylation of histone H3 at arginine 2 (H3R2me2a). This mark has been reported to associate with silent genes. Here, we use a cell model of neural differentiation, which upon PRMT6 knockout exhibits proliferation and differentiation defects. Strikingly, we detect PRMT6-dependent H3R2me2a at active genes, both at promoter and enhancer sites. Loss of H3R2me2a from promoter sites leads to enhanced KMT2A binding and H3K4me3 deposition together with increased target gene transcription, supporting a repressive nature of H3R2me2a. At enhancers, H3R2me2a peaks co-localize with the active enhancer marks H3K4me1 and H3K27ac. Here, loss of H3R2me2a results in reduced KMT2D binding and H3K4me1/H3K27ac deposition together with decreased transcription of associated genes, indicating that H3R2me2a also exerts activation functions. Our work suggests that PRMT6 via H3R2me2a interferes with the deposition of adjacent histone marks and modulates the activity of important differentiation-associated genes by opposing transcriptional effects.

## INTRODUCTION

A multitude of nuclear and cytoplasmic proteins are posttranslationally modified by arginine methylation. Arginines frequently contribute to intermolecular interactions due to hydrogen-bonding and amino-aromatic interactions. Methylation of such pivotal arginine residues modulates the binding affinity between interaction partners leading to promotion or inhibition of interactions (Gayatri and Bedford, 2014). The enzymes responsible for this modification are protein arginine methyltransferases (PRMTs), which constitute an enzyme family of nine members in mammals (Yang and Bedford, 2013). They transfer methyl groups from the ubiquitous methyl-group donor S-adenosyl-L-methionine (SAM) to the terminal guanidino nitrogens of arginine residues, giving rise to monomethyl-arginine (MMA), asymmetric dimethyl-arginine (ADMA), or symmetric dimethyl-arginine (SDMA). PRMTs regulate a wide range of essential cellular processes, for example, signal transduction, nucleo-cytoplasmic transport, transcriptional regulation, RNA splicing, and DNA repair (Yang and Bedford, 2013).

Our previous studies identified asymmetric dimethylation of histone H3 at arginine 2 (H3R2me2a) as the predominant histone mark catalyzed by the family member PRMT6 (Hyllus et al., 2007). H3R2me2a was found to contribute to gene repression by blocking the catalytic activity of the H3K4 methyltransferase KMT2A and counteracting the formation of H3K4 trimethylation (Guccione et al., 2007; Hyllus et al., 2007; Iberg et al., 2008;



Kirmizis et al., 2007; Michaud-Levesque and Richard, 2009; Stein et al., 2012). In agreement with these observations, H3R2me2a was shown to be depleted from active genes and present at genomic regions with low H3K4me3 occupancy, such as silent genes and heterochromatin (Barski et al., 2007; Rosenfeld et al., 2009). Transcriptional repression by PRMT6 and H3R2me2a was reported to be relevant for pluripotency, differentiation processes, as well as maintenance of fully differentiated cells in various tissues (Dhawan et al., 2011; Lee et al., 2012; Stein et al., 2016). Given that until now our understanding of the gene-regulatory functions of H3R2me2a derived from analyses of individual genes and subsets of genomic loci, we investigated here the PRMT6-dependent transcriptome and genomic distribution of H3R2me2a in an unbiased and genome-wide manner. Moreover, we studied the putative cross talk between H3R2me2a and neighboring histone marks, such as H3K4 methylation (H3K4me1 and H3K4me3), H3K27 methylation (H3K27me3), and H3K27 acetylation (H3K27ac).

For these studies, we used the human embryonal carcinoma cell line NT2/D1, which is pluripotent and differentiates into neural precursor cells upon treatment with *all-trans* retinoic acid (ATRA) (Lee and Andrews, 1986). We chose this model since PRMT6 knockdown causes alterations in the transcriptional program of undifferentiated as well as ATRA-induced NT2/D1 cells (Hyllus et al., 2007; Stein et al., 2016). PRMT6 wild-type and knockout NT2/D1 cells were employed in chromatin immunoprecipitation-sequencing (ChIP-seq) and RNA-sequencing (RNA-seq) analyses. In contrast to our expectations, we found that H3R2me2a is deposited in a PRMT6-dependent manner primarily at active genes, both at promoter and enhancer sites. Here, H3R2me2a seems to contribute to the transcriptional regulation of important pluripotency and differentiation-associated genes by influencing the deposition of neighboring histone marks. Our data support the concept that arginine methylation exerts its regulatory activity by modulating protein-protein interactions. Depending on its genomic location, H3R2me2a possesses either a repressive or activating nature: transcriptional repression at promoters and transcriptional activation at enhancers.

## RESULTS

### PRMT6-Dependent H3R2me2a Is Predominantly Deposited at TSS and Promoter Regions in Undifferentiated NT2/D1 Cells

By combining genome-wide analyses on the H3R2me2a deposition profile (ChIP-seq) and the PRMT6-dependent transcriptome (RNA-seq), we aimed to elucidate the functional and mechanistic impact of PRMT6 and its major histone mark in gene regulation. We used CRISPR/Cas9 genome editing to generate PRMT6 knockout (KO) and control (CT) NT2/D1 cells. NT2/D1 KO cell lines showed a complete loss of PRMT6 expression and a global reduction of arginine methylated proteins in comparison to CT cells (Figure 1A). Furthermore, we generated an antibody, which specifically recognizes the H3R2me2a modification, also in presence of the neighboring H3K4me3 mark (Figures S1A–S1E). Monomethylated H3R2 (H3R2me1) was weakly detected by the antibody, whereas unmethylated H3R2 (H3R2me0), symmetrically dimethylated H3R2 (H3R2me2s), and other methylation

marks of the H3 as well as H4 N terminus were not recognized (Figures S1A–S1E). We performed ChIP-seq using this antibody and obtained in undifferentiated NT2/D1 CT cells a total of 2,300 binding sites, as visualized by heatmap (Figure 1B). In contrast, ChIP-seq datasets of two NT2/D1 KO cell lines revealed a strong reduction of H3R2me2a signals indicating that these 2,300 sites are PRMT6 dependent (Figures 1B and S1F). Analysis of the relative genomic distribution of the H3R2me2a sites showed that 72% of these occur in the vicinity of transcriptional start sites (TSSs) (Figure 1C). To validate these ChIP-seq results, we selected candidate loci, as depicted in the genome browser views for NT2/D1 CT and KO cells (Figures 1D and S1G). Using independent ChIP-qPCR assays, we confirmed the H3R2me2a occupancy at these loci in undifferentiated NT2/D1 CT cells as well as the loss of H3R2me2a enrichment upon PRMT6 deletion (Figures 1E and S1H). Control regions in proximity to H3R2me2a binding sites revealed background signal of H3R2me2a in NT2/D1 CT and KO cells (Figure 1E). Native ChIP analysis in CT cells reproduced the H3R2me2a binding sites (Figure S1I). Furthermore, re-expression of PRMT6 in KO cells resulted in the re-establishment of H3R2me2a occupancy (Figures S2A–S2D). Hence, these results uncover the genome-wide binding profile of PRMT6-dependent H3R2me2a in pluripotent NT2/D1 cells. The predominant TSS and promoter-proximal distribution of H3R2me2a suggests that this mark is likely involved in the regulation of gene expression.

### H3R2me2a Deposition Displays Three Distinct Patterns during ATRA-Induced NT2/D1 Cell Differentiation

Next, we analyzed the dynamics of H3R2me2a deposition during NT2/D1 cell differentiation upon ATRA treatment. A total of 8,819 unique H3R2me2a binding sites was detected by ChIP-seq in undifferentiated and differentiated NT2/D1 CT cells, which encompassed the 2,300 peaks of undifferentiated cells and additional 6,519 peaks acquired upon differentiation. Based on their enrichment in the minus-ATRA and plus-ATRA conditions, we divided these peaks into three clusters (Figure 2A). Cluster I peaks are present in the minus-ATRA condition and are reduced or lost upon ATRA treatment, cluster II peaks are equally strong in both ATRA conditions, and cluster III peaks show a gain of H3R2me2a enrichment upon ATRA-induced differentiation. In NT2/D1 KO cells, the peaks of all three clusters were significantly reduced (Figure 2A). Using gene ontology (GO) analysis, we found that genes associated with the three different peak clusters execute distinct and essential functions in NT2/D1 cells (Figure 2B). Cluster I-associated genes were predominantly annotated to terms such as axon guidance, stem cell maintenance, and pluripotency, as exemplified by the genes *OCT4*, *NANOG*, *ID1*, and *REST*, which are downregulated upon neural differentiation (Figure 2B). Cluster II genes, e.g., *ST3GAL2*, *MITF*, *FASTKD1*, *CNOT1*, and *LARS*, revealed as overrepresented GO terms cell cycle, RNA processing, chromatin organization, DNA damage response, and posttranslational modifications (PTMs). These peaks showed particularly robust enrichment, as validated in Figure 1E, and associate with genes that are not responsive to ATRA treatment (Figure 2B). In cluster III, the overrepresented GO terms were cell cycle, CNS development, and neurogenesis. Gene examples are the *HOXA* cluster, *RARB*, *VTCN1*, *CRABP1*, and

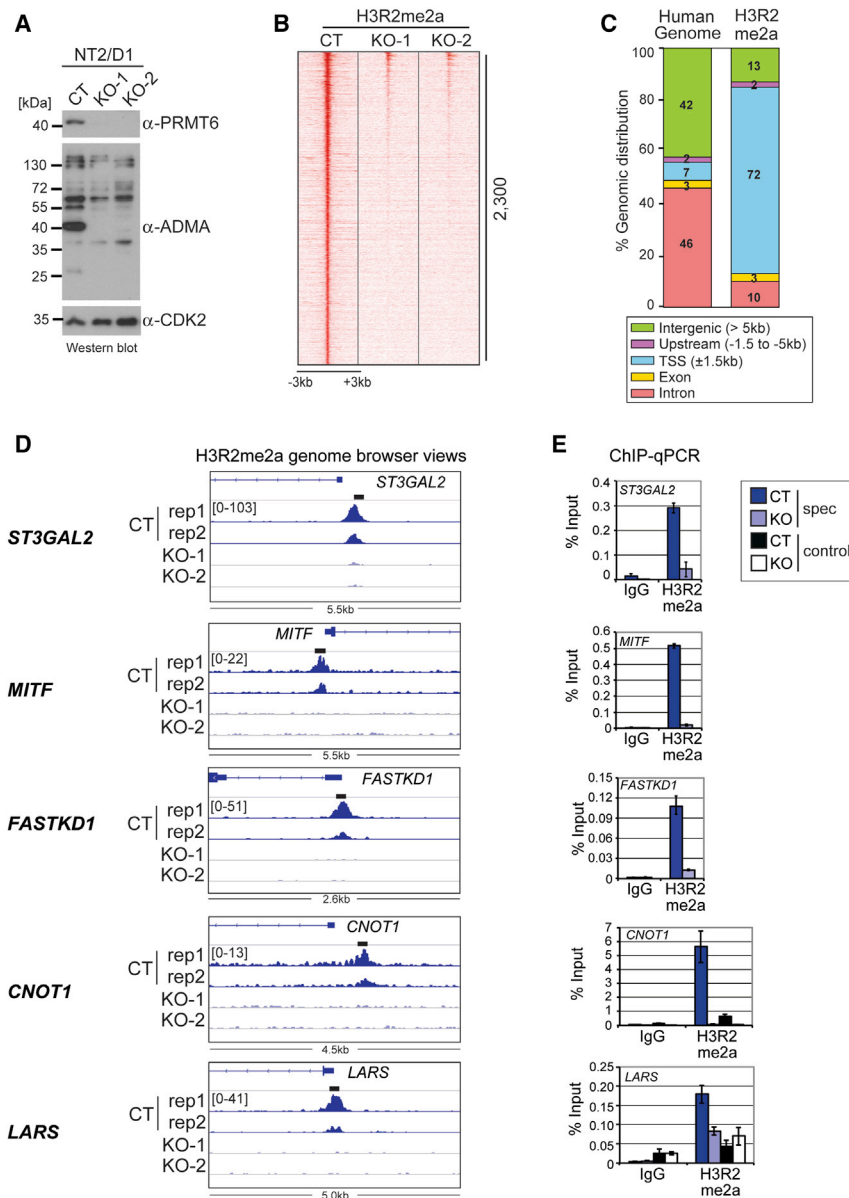


**Figure 1. PRMT6-Dependent and Promoter-Proximal Deposition of H3R2me2a in NT2/D1 Cells**

(A) Protein extracts of undifferentiated control (CT) or PRMT6-deleted (KO-1, KO-2) NT2/D1 cell lines were analyzed by western blot using the indicated antibodies ( $\alpha$ -PRMT6,  $\alpha$ -ADMA,  $\alpha$ -CDK2). CDK2 staining served as loading control. Size markers (in kilodaltons) are shown on the left.

(B) Heatmap displays the H3R2me2a ChIP-seq signals in undifferentiated NT2/D1 CT cells over the 2,300 binding sites sorted in the descending order of their signal strength ( $\pm 3$  kb around the centered summits) in comparison to H3R2me2a ChIP-seq profiles of NT2/D1 KO-1 and KO-2 cell lines.

(C) Relative distribution of the 2,300 H3R2me2a peaks (of B) is shown within different genomic regions compared to the distribution of these regions in the human genome.

(D) Genome browser views of H3R2me2a ChIP-seq datasets of NT2/D1 CT (two replicates) and both KO cell lines are shown for five gene loci. Positions of amplicons (spec, specific region) generated by qPCR (E) are depicted as black boxes above the top browser tracks. Data range is indicated in brackets.

(E) ChIP-qPCR assays were performed in NT2/D1 CT and KO cells (=KO-2, which we employed in all subsequent experiments as PRMT6 knockout cell line) using control antibodies (IgG) and  $\alpha$ -H3R2me2a. Precipitated DNA was analyzed by qPCR with primers amplifying the H3R2me2a peaks (spec) or a nearby control region (control) of the depicted loci. Amplicons for control regions are in case of *CNOT1* 16 kb downstream of TSS in intron 1 and in case of *LARS* 18 kb downstream of TSS in exon 6. Recruitment is displayed in percent input of chromatin; mean  $\pm$  SD of triplicates.

*ARID1A*, which are predominantly upregulated upon ATRA treatment (Figure 2B). In ChIP-qPCR and RT-qPCR assays, we validated several candidate genes of the three clusters for their H3R2me2a occupancy and transcriptional characteristics in undifferentiated and ATRA-treated NT2/D1 CT cells, such as *OCT4* and *ID1* for cluster I, *LARS* and *MITF* for cluster II, and *VTCN1* and *CRABP1* for cluster III (Figures 2C and S3A). These results demonstrate that H3R2me2a displays differentiation-dependent dynamics in NT2/D1 cells and marks genes, which exert essential functions in pluripotency, cell cycle, and neural differentiation.

### H3R2me2a Co-localizes with Other Histone H3 Marks and Associates with Active Genes

Given that H3R2me2a has been reported to influence the occurrence of adjacent histone H3 modifications, in particular

H3K4me3 (Guccione et al., 2007; Hyllus et al., 2007), we analyzed the distribution of this promoter mark in undifferentiated and differentiated NT2/D1 CT cells by ChIP-seq. Surprisingly, we found that 48% (4,236 peaks) of the total 8,819 H3R2me2a sites overlap with a high occupancy of H3K4me3 but not with H3K27me3, suggesting that H3R2me2a is mainly present at non-bivalent, active gene promoters (Figures 2D, S3B, and S3C). No global changes in the H3K4me3 occupancy were observed when comparing minus/plus-ATRA conditions. Genes of all three clusters contributed to this group of promoter-associated H3R2me2a peaks. The remaining 4,538 H3R2me2a sites displayed very low occupancy of H3K4me3 (Figure 2D) and high enrichment of non-TSS regions (data not shown). This prompted us to examine the distribution of two enhancer modifications, H3K4me1 and H3K27ac. H3K4me1 alone marks primed enhancers, whereas H3K4me1 in conjunction with H3K27ac characterizes active enhancers (Calo and Wysocka, 2013). Interestingly, we observed that the remaining 52% H3R2me2a binding sites predominantly co-occur with sites of high H3K4me1 and H3K27ac occupancy,



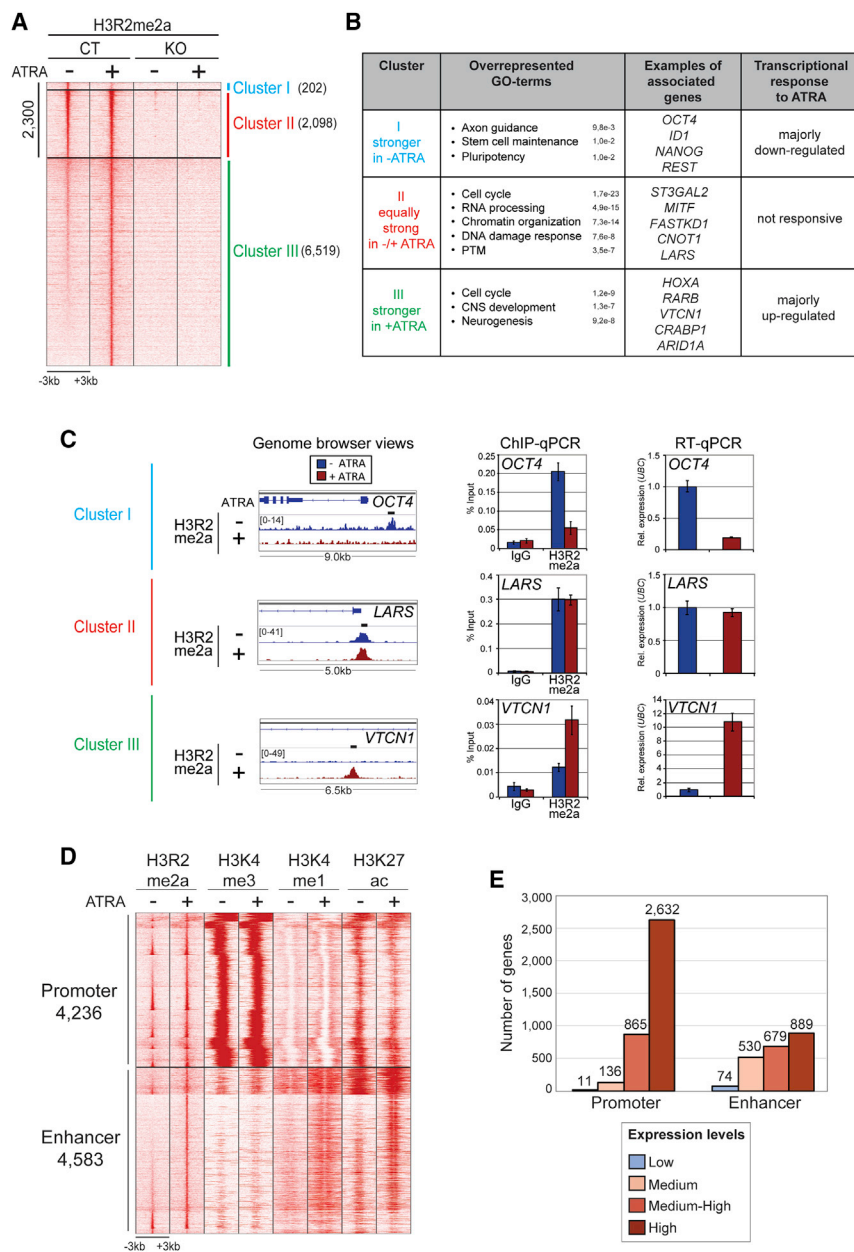


**Figure 2. Dynamics of the Genome-wide H3R2me2a Deposition during NT2/D1 Cell Differentiation and Co-occurrence of H3R2me2a with Other Histone H3 Marks**

(A) Heatmap of H3R2me2a ChIP-seq binding profile ( $\pm 3$  kb around the centered peak summits) in NT2/D1 CT versus KO cells minus/plus ATRA at 8,819 genomic loci. Peaks are divided into three clusters (I, II, and III) depending on their H3R2me2a enrichment in the minus- and plus-ATRA conditions.

(B) Table summarizing the characteristics of genes associated with H3R2me2a binding sites of the three clusters. Overrepresented GO terms and their corresponding q values are indicated.

(C) Genome browser views of the H3R2me2a ChIP-seq datasets of NT2/D1 CT cells minus/plus ATRA are depicted for gene loci illustrating the three clusters (left panels): *OCT4* (cluster I), *LARS* (cluster II), and *VTCN1* (cluster III). Positions of amplicons generated by qPCR are depicted as black boxes above the top browser tracks. Data range is indicated in brackets. ChIP-qPCR assays were performed using control antibodies (IgG) and  $\alpha$ -H3R2me2a and primers amplifying the H3R2me2a peaks of the depicted loci. Recruitment is displayed in percent input of chromatin; mean  $\pm$  SD of triplicates (middle panels). Total RNA was analyzed by RT-qPCR for the transcript levels derived from three gene loci. Values were normalized to *UBIQUITIN (UBC)* expression and presented relative to the minus-ATRA condition; mean  $\pm$  SD of triplicates (right panels).

(D) Heatmap displays the H3R2me2a ChIP signals over 8,819 sites in comparison to ChIP-seq profiles of histone marks (H3K4me3, H3K4me1, and H3K27ac) in NT2/D1 CT cells minus/plus ATRA, as regions classified in promoters (4,236 sites) or enhancers (4,583 sites) based on the signal strength of their specific histone marks.

(E) RNA-seq analysis was performed in NT2/D1 CT cells plus ATRA. Genes associated with H3R2me2a binding sites either at their promoter or enhancer were binned according to their transcriptional strength in four categories based on expression quantiles (normalized as TPM [transcript per million reads per kilobase]): low,  $<0.09$  and  $>0$ ; medium,  $<0.84$  and  $\geq 0.09$ ; medium-high,  $<10.5$  and  $\geq 0.84$ ; high,  $>10.5$ .

indicating that here H3R2me2a localizes with active enhancer regions (Figure 2D). These enhancer-associated H3R2me2a binding sites showed an increase in H3K4me1 and H3K27ac occupancy concomitant to the gain in H3R2me2a enrichment upon ATRA treatment. Over 80% of the H3R2me2a enhancer sites belong to cluster III. To address whether the here-observed H3R2me2a deposition feature is a cell-type-specific phenomenon, we performed ChIP-seq analysis of this mark in the human osteosarcoma cell line U2OS with either wild-type levels of PRMT6 (CT) or PRMT6 KO. Thereby, we identified 3,253 PRMT6-dependent H3R2me2a sites, of which 47% (1,556 peaks) overlapped with peaks in NT2/D1 cells (Figures S4A–S4F). Interestingly, as observed in NT2/D1 cells, H3R2me2a

sites in U2OS cells were co-occupied by H3K4me3 or H3K4me1/H3K27ac (Figure S4G). Thus, our results indicate that the co-occurrence of H3R2me2a with these other H3 marks is a general and cell-type-independent characteristic.

To determine the transcriptional output of genes with either promoter- or enhancer-deposited H3R2me2a in NT2/D1 cells, we performed RNA-seq analyses. We then binned all H3R2me2a-associated unique genes (6,697) according to their transcription levels in differentiated CT cells. We found that H3R2me2a at promoters predominantly marks highly transcribed genes, whereas H3R2me2a at enhancers is located in proximity to genes distributed in all four categories of expression levels (Figure 2E). Our observations were unexpected, since up

to now PRMT6 and H3R2me2a have been reported to mainly associate with silent genes (Guccione et al., 2007; Hyllus et al., 2007; Iberg et al., 2008; Kirmizis et al., 2007). Altogether, these results reveal that H3R2me2a possesses two distinct locations in the genome, at promoter and enhancer sites. At both locations, H3R2me2a co-occurs with active histone modifications and consistently marks primarily active genes.

### H3R2me2a Contributes to Activation as well as Repression of Associated Genes

To address whether H3R2me2a influences the transcriptional output of the associated genes, we compared the PRMT6-dependent transcriptome of NT2/D1 CT and KO cells by RNA-seq. We identified 710 differentially expressed genes in ATRA-stimulated cells (Figure S5A). These deregulated genes were almost equally distributed into the upregulated and downregulated groups, respectively (374 upregulated genes and 336 downregulated genes). To distinguish direct from indirect transcriptional effects of PRMT6-dependent H3R2me2a, we combined our ChIP-seq and RNA-seq datasets. This analysis showed that approximately 25% of deregulated genes (176 genes) harbor H3R2me2a binding sites in their proximity. A larger number of genes with enhancer-deposited H3R2me2a was deregulated compared to genes with promoter-deposited H3R2me2a (Figure S5B). The majority of these direct H3R2me2a targets (70%) were downregulated upon PRMT6 knockout, indicating that PRMT6-dependent H3R2me2a predominantly contributes to transcriptional activation of associated genes. This effect was more pronounced for genes associated with H3R2me2a enhancer peaks (Figure S5B). Altogether, our results indicate that H3R2me2a contributes to gene repression as well as gene activation, the latter accounting for the majority of effects.

### Promoter-Associated H3R2me2a Attenuates H3K4me3 Occupancy and Transcriptional Activity

We next investigated whether promoter-associated H3R2me2a influences the deposition of H3K4me3 and the transcriptional output of the associated genes. Thus, we plotted the intensity of H3K4me3 signals in NT2/D1 CT versus KO cells and found that the H3K4me3 occupancy of upregulated genes is significantly increased upon PRMT6 knockout (Figures 3A and S5C). On the contrary, the downregulated genes showed no significant difference in the H3K4me3 deposition between CT and KO cells. Our findings suggest that PRMT6 and H3R2me2a negatively influence H3K4me3 deposition at the chromatin. Independent ChIP-qPCR verified the higher occupancy of H3K4me3 for genes of all three clusters in PRMT6-deficient cells (Figures 3B and S5D). Moreover, this increase in H3K4me3 occupancy coincided with an elevated transcriptional activity (Figures 3C and S5D) and an enhanced KMT2A binding to these H3R2me2a target genes in KO cells (Figure 3D). Our data indicate that promoter-associated H3R2me2a possesses a repressive nature by interfering with the recruitment of KMT2A and antagonizing the deposition of H3K4me3. However, in contrast to previous perceptions (Guccione et al., 2007; Hyllus et al., 2007; Iberg et al., 2008), this repressive function of H3R2me2a does not occur at silent gene loci, but rather at active genes, causing a restraint of their tran-

scriptional output. Thus, H3R2me2a localized at promoters leads to fine-tuning of transcriptional activities and impedes unauthorized high expression of pluripotency genes (cluster I, Figure 2B) as well as differentiation-associated genes (cluster III, Figure 2B) in NT2/D1 cells.

### Enhancer-Associated H3R2me2a Promotes the Deposition of H3K4me1/H3K27ac and the Transcriptional Activation of Corresponding Genes

To investigate the role of enhancer-associated H3R2me2a binding sites, we plotted these peaks according to their affiliation to cluster I, II, and III in NT2/D1 CT and KO cells and compared them to the ChIP-seq profiles of H3K4me3, H3K4me1, and H3K27ac (Figure 4A). As mentioned above, enhancer-associated H3R2me2a peaks mainly belong to cluster III (i.e., increased peak intensity in plus ATRA) and generally show very low occupancy of H3K4me3. Strikingly, deposition of H3K4me1 and H3K27ac resembled the occurrence of H3R2me2a at cluster III genes. The occupancy of both enhancer marks clearly augmented upon differentiation of NT2/D1 CT cells (comparing CT minus/plus ATRA, Figures 4A and 4B). This ATRA-induced increase was significantly diminished upon deletion of PRMT6 (comparing CT and KO, both plus ATRA), suggesting that the differentiation-associated depositions of H3R2me2a and the two enhancer marks are connected. This assumption was supported by the facts that PRMT6 knockout had a very moderate impact on the H3K4me1/H3K27ac occupancy in undifferentiated cells (comparing CT and KO, both minus ATRA), and further that the ATRA-induced increased deposition of enhancer marks was only marginally detectable in KO cells (comparing KO minus/plus ATRA, Figures 4A and 4B). Moreover, we observed a strong positive correlation between the enrichment levels of H3R2me2a and both enhancer marks in differentiating CT cells (Figures S6A and S6B). Collectively, our findings point to an H3R2me2a-dependent deposition mechanism of these enhancer histone marks.

The H3K4 mono-methyltransferase KMT2D contains several PHD fingers, of which PHD<sub>4-6</sub> are well-known reader domains of histone H4 (Dhar et al., 2012). We investigated here whether KMT2D also binds to the histone H3 tail and whether this binding is influenced by H3R2me2a. Therefore, we performed peptide pull-down assays using either recombinant GST-KMT2D purified from bacteria or Flag-KMT2D overexpressed in cell lysates. By means of wild-type and mutant KMT2D proteins, we found that PHD<sub>4-6</sub> of KMT2D, in particular PHD<sub>6</sub>, possess binding preferences for H3R2me1 and H3R2me2a peptides, but not for H3R2me0, H3R2me2s, or H3R17me2a (Figures 4C, S6C, and S6D). In agreement with these findings, ChIP-seq analysis of KMT2D in NT2/D1 CT and KO cells showed a co-occurrence of H3R2me2a and KMT2D (Figures 4A, 4B, and S6E–S6I). Furthermore, we detected a positive correlation of H3R2me2a and KMT2D enrichment levels at the chromatin and, importantly, a dependence of KMT2D binding on H3R2me2a deposition (Figures S6G–S6I). Our data suggest that PRMT6 facilitates the deposition of H3K4me1 potentially in a direct manner by enhancing chromatin recruitment of the KMT2D complex, which has been reported to promote p300-dependent H3K27 acetylation (Wang et al., 2016, 2017).

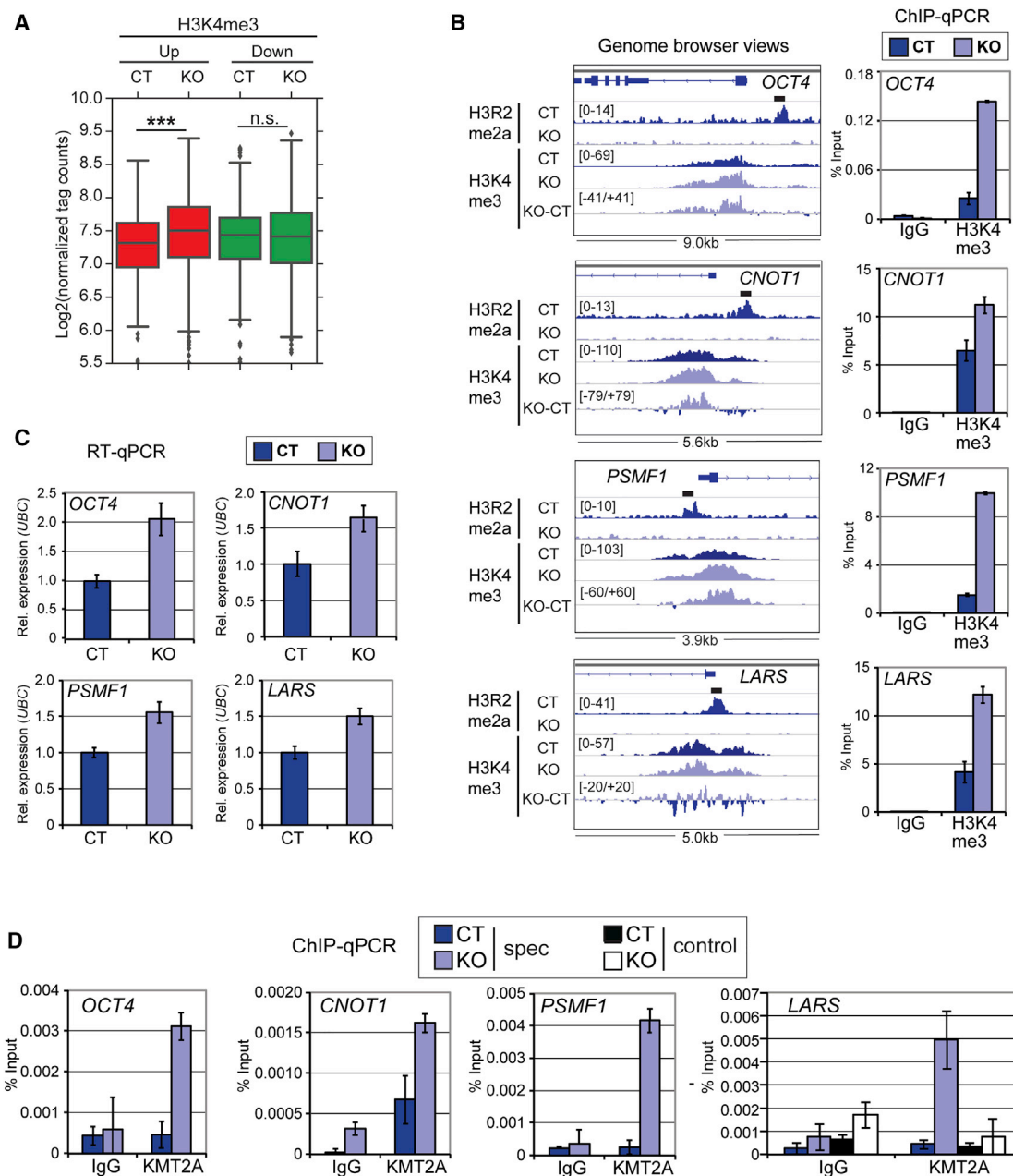


**Figure 3. Negative Influence of Promoter-Associated H3R2me2a on H3K4me3 Deposition and Transcriptional Activity of Target Genes**

(A) Boxplot analysis presents the normalized H3K4me3 tag counts for upregulated (red boxes) and downregulated genes (green boxes) in NT2/D1 CT and KO cells. \*\*\* $p \leq 0.001$ ; n.s.: not significant using Welch's t test.

(B) Genome browser views of the H3R2me2a and H3K4me3 ChIP-seq datasets generated in NT2/D1 CT and KO cells are shown for the indicated gene loci (left panels). H3K4me3 signal differences between NT2/D1 KO and CT are illustrated in a separate track (KO-CT). Positions of amplicons generated by qPCR are depicted as black boxes above the top browser tracks. Data range is indicated in brackets. ChIP-qPCR assays were performed in NT2/D1 CT and KO cells using control antibodies (IgG) or  $\alpha$ -H3K4me3 and primers encompassing the H3R2me2a peaks of the different loci. Recruitment is displayed in percent input of chromatin; mean  $\pm$  SD of triplicates (right panels).

(C) Total RNA of NT2/D1 CT and KO cells was analyzed by RT-qPCR for transcript levels of the indicated genes (studied in B). Values were normalized to *UBIQUITIN* (*UBC*) expression and presented relative to NT2/D1 CT cells; mean  $\pm$  SD of triplicates.

(D) ChIP-qPCR assays were performed in NT2/D1 CT and KO cells using control antibodies (IgG) or  $\alpha$ -KMT2A and primers encompassing the H3R2me2a peaks (spec, specific region) of the different loci (studied in B) as well as a control region for *LARS* (=control; 18 kb downstream of TSS in exon 6). Recruitment is displayed in percent input of chromatin; mean  $\pm$  SD of triplicates.







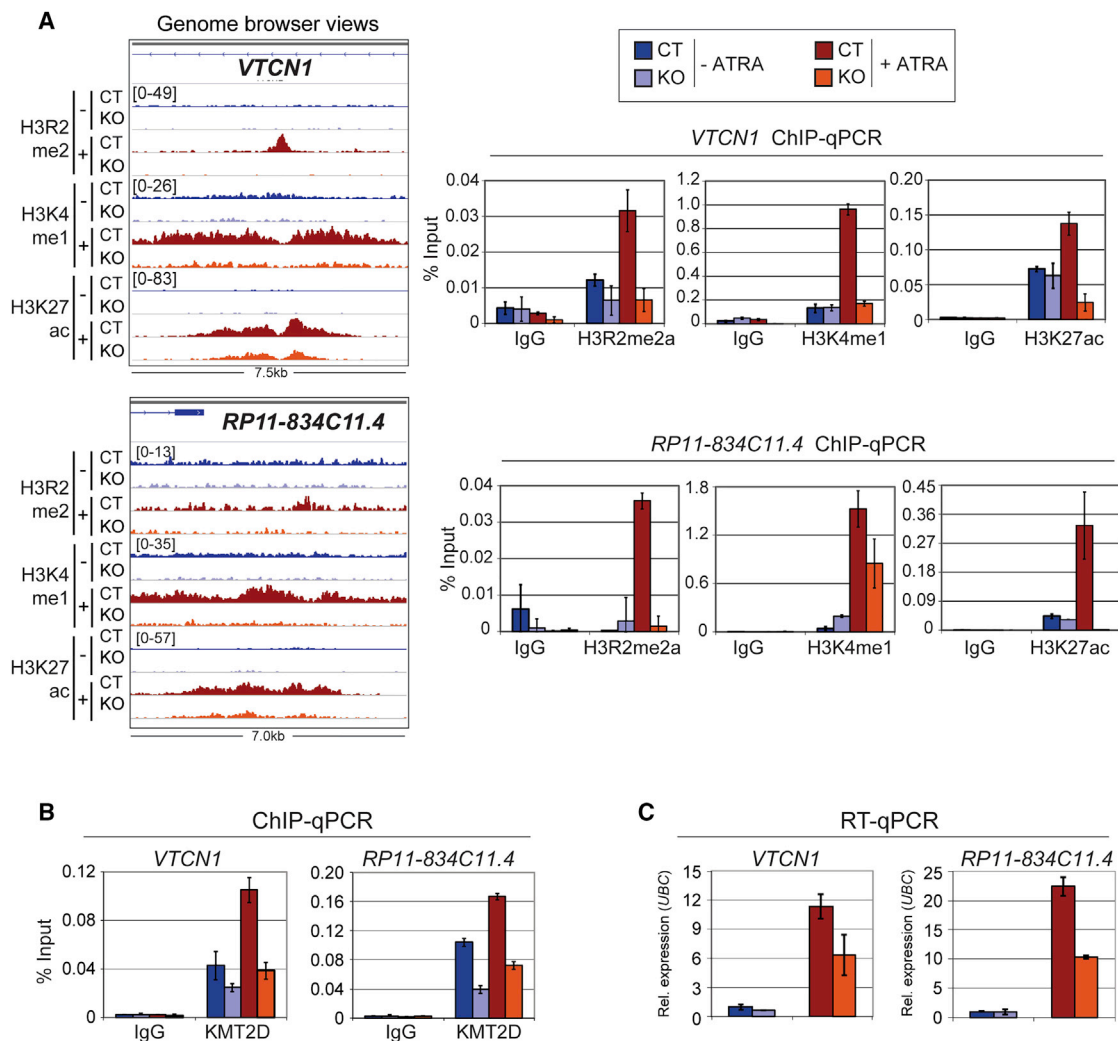


**Figure 5. Transcriptional Activation Due to Enhancer-Associated H3R2me2a**

(A) Genome browser views are shown for the indicated cluster III genes of H3R2me2a, H3K4me1, and H3K27ac ChIP-seq datasets generated in NT2/D1 CT and KO cells minus/plus ATRA (left panels). Data range is indicated in brackets. ChIP-qPCR assays were performed in NT2/D1 cells using the indicated antibodies and primers encompassing the histone modification peaks of the different loci. Recruitment is displayed in percent input of chromatin; mean  $\pm$  SD of triplicates (right panels).

(B) ChIP-qPCR assays, as described in (A), were performed for KMT2D in NT2/D1 cells. The color code of the four conditions is displayed in (A).

(C) Transcript levels of the indicated cluster III genes (studied in A) were analyzed by RT-qPCR in NT2/D1 CT and KO cells minus/plus ATRA. The color code of the four conditions is displayed in (A). Values were normalized to *UBIQUITIN* (*UBC*) expression and presented relative to NT2/D1 CT cells minus ATRA; mean  $\pm$  SD of triplicates.

(comparing CT minus/plus ATRA, Figure 4D). In contrast, in KO cells, ATRA treatment did not result in any significant increase in transcript levels of these genes (comparing KO minus/plus ATRA, Figure 4D). Importantly, comparing CT and KO in plus ATRA, PRMT6 knockout led to a loss of the differentiation-dependent transcriptional activation (Figure 4D). Besides, a heatmap of these transcriptional changes revealed that the very same genes, which were activated upon ATRA treatment in CT cells, lost their transcriptional response upon PRMT6 knockout (Figure 4E). Independent ChIP-qPCR and RT-qPCR assays of candidate cluster III genes, such as *VTCN1*, *RP11-834C11.4*, and *CRABP1*, validated the

effects of PRMT6 deletion on H3K4me1/H3K27ac deposition, KMT2D recruitment, as well as transcriptional output (Figures 5A–5C and S7A). Moreover, re-expression of PRMT6 in NT2/D1 KO cells (Figure S2A) resulted in a rescue of the ATRA-induced H3K27ac deposition and differentiation-dependent transcriptional activation of associated genes (Figure S7B). Hence, our findings reveal that enhancer-associated H3R2me2a is predominantly deposited in a differentiation-dependent manner in NT2/D1 cells. There, it possibly promotes the deposition of H3K4me1 and H3K27ac, by recruitment of KMT2D, and thus enables transcriptional activation upon neural differentiation.

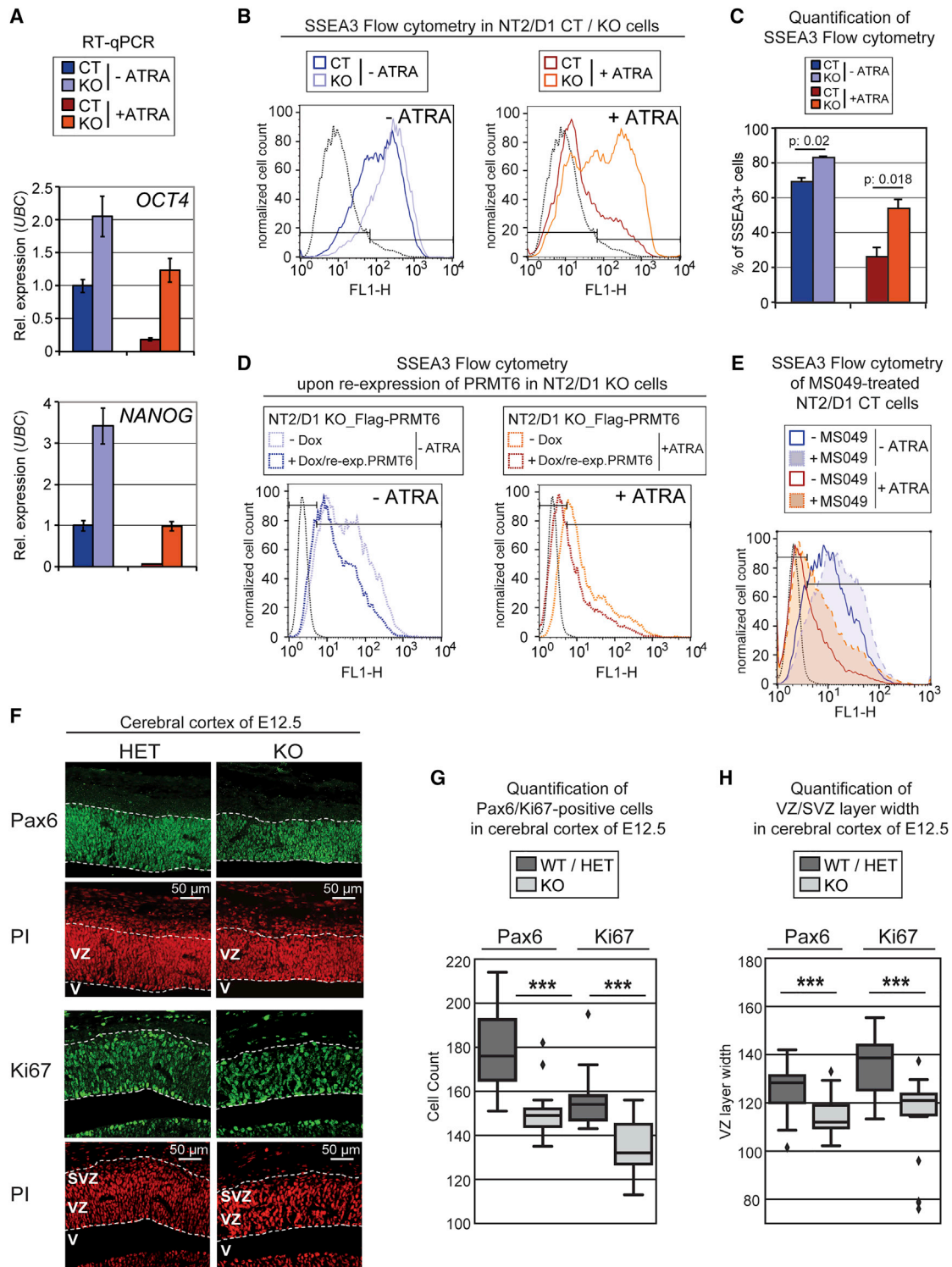


**Figure 6. Impact of PRMT6 on Neural Differentiation and Proliferation *In Vitro* and *In Vivo***

(A) Transcript levels of *OCT4* and *NANOG* were analyzed by RT-qPCR in NT2/D1 CT versus KO cells minus/plus ATRA. Values were normalized to *UBIQUITIN* (*UBC*) expression and presented relative to NT2/D1 CT cells minus ATRA; mean  $\pm$  SD of triplicates.

(B and C) The fraction of SSEA3-positive and SSEA3-negative cells was measured by flow cytometry of NT2/D1 CT and KO cells in minus- and plus-ATRA conditions. HeLa cells (black dotted line) served as negative control to define gates of SSEA3-positive and SSEA3-negative cells (black bars). (B) shows an

(legend continued on next page)

### PRMT6 Influences the Differentiation and Proliferation Capacity of NT2/D1 Cells and of Neural Precursor Cells in the Developing Mouse Cortex

Given the enhanced expression of pluripotency-associated genes in NT2/D1 KO cells before and after ATRA treatment, as illustrated for *OCT4* and *NANOG* (Figure 6A), we raised the question whether PRMT6 influences the differentiation capacity of NT2/D1 cells. Undifferentiated NT2/D1 cells express the cell surface marker SSEA3, which indicates their stem cell-like state (Houldsworth et al., 2002). Using flow cytometry, we found that a higher percentage of NT2/D1 KO cells is SSEA3-positive and thus more pluripotent in the undifferentiated condition compared to CT cells (Figures 6B and 6C). Upon ATRA treatment, this difference was even more pronounced, suggesting that PRMT6 knockout leads to reduced neural differentiation. Additionally, undifferentiated NT2/D1 KO cells displayed a prolonged G1 phase and diminished proliferation rate (S phase) compared to CT cells, as measured by flow cytometry using propidium iodide staining (Figure S8A). These proliferation and differentiation defects of KO cells were rescued upon re-expression of PRMT6, which restored a higher number of cells in S phase, a reduced percentage of pluripotent (SSEA3-positive) cells in the minus-ATRA condition and an increased fraction of differentiating (SSEA3-negative) cells upon ATRA treatment (Figures 6D, S8B, and S8C). To further address whether the catalytic activity of PRMT6 is responsible for the neural differentiation phenotype of KO cells, we treated NT2/D1 CT cells with MS049, a potent PRMT6 inhibitor (Shen et al., 2016). This treatment resulted in a global reduction of arginine methylated proteins and a reduced genomic occupancy of H3R2me2a (Figures S8D–S8F). Interestingly, MS049 treatment phenocopied the defects on pluripotency and differentiation caused by PRMT6 knockout, indicating that these PRMT6-mediated functions require its catalytic activity (Figures 6E and S8G).

Since differentiating NT2/D1 cells resemble Pax6-positive neural stem cells of the developing fetal CNS (Houldsworth et al., 2002), we investigated whether *Prmt6* also influences neural differentiation *in vivo* in mice. First, we analyzed the protein expression of *Prmt6* in fetal and adult murine brain tissue. In agreement with previous studies, we found *Prmt6* to be highly expressed in the developing mouse brain (McKee et al., 2005)

as well as in different regions of the adult mouse brain (Figure S8H). Given that Pax6-positive as well as proliferating (Ki67-positive) neural progenitor cells are highly abundant in the mouse cerebral cortex of embryonic day 12.5 (E12.5), we quantified the progenitor numbers of this developmental stage in wild-type (WT) and heterozygous (HET) versus *Prmt6* KO mice (Neault et al., 2012). Thereby, we identified that the numbers of Pax6-positive and Ki67-positive progenitors, respectively, as well as the layer widths of the ventricular zone (VZ) and subventricular zone (SVZ) are reduced in the cerebral cortex of *Prmt6* KO embryos compared to WT and HET embryos (Figures 6F–6H). At later developmental stages and in the adult murine brain, we did not find significant differences in the number of neurons and in the morphology of the brain between WT/HET and KO animals (data not shown). Our observations are consistent with the inconspicuous phenotype of *Prmt6* KO mice (Neault et al., 2012). We hypothesize that the important *in vivo* functions of *Prmt6* are partially compensated in the KO mouse model by other *Prmt* members. Hence, these findings show that PRMT6-deficient neural cells display a very stable stem cell-like state and a perturbation of their proliferation and differentiation capacity in an *in vitro* cell model as well as *in vivo*. Additional mechanisms involving non-catalytic functions and other substrates of PRMT6 could contribute to the here-described effects of PRMT6 knockout.

In summary, our data identify PRMT6 as a regulator of neural differentiation that seems to influence the transcription program of neural precursors, as exemplified here for NT2/D1 cells, at least in two ways: promoter-associated H3R2me2a diminishes the transcription of critical pluripotency genes, whereas enhancer-associated H3R2me2a promotes transcriptional activation of differentiation-associated genes.

### DISCUSSION

To investigate the gene-regulatory functions of PRMT6 and its major histone mark H3R2me2a in an unbiased and genome-wide manner, we established CRISPR/Cas9-mediated deletion of PRMT6 in the human embryonal carcinoma cell line NT2/D1. In this well-established cell model, PRMT6 has previously been shown to regulate the ATRA-induced transcription program of

exemplary experiment. (C) displays the quantification of SSEA3-positive (SSEA3<sup>+</sup>) cells of three independent experiments. The p values are indicated using Welch's t test.

(D) NT2/D1 KO\_Flag-PRMT6 cells were cultured in the absence or presence of PRMT6 re-expression (minus/plus doxycycline for 6 days) and minus/plus ATRA (last 3 days). The fraction of SSEA3-positive and SSEA3-negative cells was measured by flow cytometry. HeLa cells (black dotted line) served as negative control to define gates of SSEA3-positive and SSEA3-negative cells (black bars). An exemplary experiment is shown. Quantification of four independent experiments is shown in Figure S8C.

(E) The fraction of SSEA3-positive and SSEA3-negative NT2/D1 CT cells either untreated or treated for 3 days with ATRA, MS049 (16  $\mu$ M), or both was measured by flow cytometry. HeLa cells (black dotted line) served as negative control to define gates of SSEA3-positive and SSEA3-negative cells (black bars). An exemplary experiment is shown. Quantification of four independent experiments is shown in Figure S8G.

(F) Cryosections of the developing murine cerebral cortex of *Prmt6*<sup>+/-</sup> (HET) or *Prmt6*<sup>-/-</sup> (KO) embryos (E12.5) were stained by immunofluorescence for Pax6 (in green) as a neural progenitor cell marker, which recognizes the abundant number of apical radial glial cells of the murine ventricular zone (VZ) at this developmental stage, for Ki67 (in green) as a marker of the proliferating progenitors (predominantly in the VZ and SVZ [subventricular zone]) and for propidium iodide (PI) (in red) as a nuclear/DNA stain. The VZ (stained by Pax6) and the VZ/SVZ (stained by Ki67) are indicated between the white dotted lines and were taken into account for cell counting (G) and layer width quantification (H). The ventricles (V) are marked.

(G and H) For quantification of progenitor cell numbers as well as VZ and VZ/SVZ layer width in the murine cerebral cortex of E12.5, Pax6- and Ki67-positive cells, respectively, of a standardized area were determined in a blinded way from five to six *Prmt6*<sup>+/-</sup> (WT) or *Prmt6*<sup>+/-</sup> (HET) and six *Prmt6*<sup>-/-</sup> (KO) embryos. The cell numbers (G) and layer width (H) of WT/HET versus KO condition are depicted as boxplot. \*\*\*p  $\leq$  0.001 using Welch's t test.

neural differentiation (Hyllus et al., 2007; Stein et al., 2016). Furthermore, PRMT6 is highly expressed in the developing mouse brain and has been suggested to influence the differentiation of embryonic stem cells (Lee et al., 2012; McKee et al., 2005). Recent studies disclosed a function of PRMT6 in the regulation of cocaine addiction in adult brain (Damez-Werno et al., 2016). Hence, using control and PRMT6 knockout NT2/D1 clones, we analyzed the impact of PRMT6-dependent H3R2me2a in pluripotency and neural differentiation. Here, PRMT6-deficient NT2/D1 cells displayed a slower growth rate compared to CT cells, in agreement with a higher number of cells in G1 phase and increased expression levels of cell cycle inhibitors such as *CDKN1A* and *CDKN2B* (data not shown). Additionally, PRMT6-deficient cells expressed more SSEA3 at their surface than their control counterparts, suggesting that, in absence of PRMT6, cells tend to retain their pluripotency state even after ATRA-induced differentiation. These findings conform with the observed cell cycle defects, since stem cells often show a low proliferation rate and a bias to quiescence (Glauche et al., 2009). Similarly, we observed reduced numbers of Pax6-positive and proliferating neural progenitors, respectively, during murine neurogenesis *in vivo*. Altogether, our data reveal that PRMT6 loss promotes the pluripotency state and perturbs the proliferation as well as differentiation capacity of NT2/D1 cells and neural precursor cells in the developing mouse brain, indicating that PRMT6 contributes to these key biological processes.

ChIP-seq profiling using anti-H3R2me2a antibodies revealed that the H3R2me2a peaks detected in NT2/D1 cells were PRMT6-dependent, as shown by the strongly reduced or lost H3R2me2a enrichment in PRMT6 knockout cells. Although PRMT6 and PRMT4 have been found to possess partially overlapping substrate specificity in certain cell types, such as mouse embryonic fibroblasts, PRMT6 seems to be the predominant methyltransferase for H3R2 in NT2/D1 cells (Torres-Padilla et al., 2007). In previous studies, we and others found that H3R2me2a mainly contributes to gene repression and occurs at silent genes (Guccione et al., 2007; Hyllus et al., 2007; Iberg et al., 2008). Intriguingly, we identified here that H3R2me2a is primarily deposited at active genes in NT2/D1 cells, both at promoter and enhancer sites. This apparent discrepancy is likely due to the fact that the hitherto-existing knowledge was predominantly obtained from analyses of individual genes and lacked unbiased genome-wide approaches to map the PRMT6-dependent H3R2me2a deposition as well as its cross talk with neighboring histone marks. Our attempts to also identify the PRMT6 binding sites in NT2/D1 cells by ChIP-seq unfortunately failed. All currently commercially available and in-house-generated PRMT6 antibodies did not efficiently immunoprecipitate PRMT6 from chromatin. Based on these observations and the fact that our in-house-generated antibodies showed specific though weak enrichment of chromatin-bound PRMT6 (Hyllus et al., 2007; Stein et al., 2012, 2016), we conclude that PRMT6 is a very dynamic nuclear protein, which transiently interacts with chromatin and therefore might escape detection, even when using double-cross-linking ChIP strategies.

Our analysis of the PRMT6-dependent transcriptome in NT2/D1 cells showed that 25% of deregulated genes associate with H3R2me2a binding sites in their proximity and are regarded as

direct targets of H3R2me2a. Strikingly, the majority of these genes were downregulated, indicating a predominant transcriptional activating function of the mark. These findings are in agreement with studies reporting an activating role of PRMT6, e.g., in nuclear hormone receptor-dependent transcription (Harison et al., 2010). The remaining genes, which are not marked by H3R2me2a, but show an altered transcriptional output upon PRMT6 deletion, are likely regulated by different mechanisms. This notion is in agreement with the findings that PRMT6 methylates several other substrates at the chromatin, for example, histone H3 at other arginines (H3R42), other histones (H2A, H4), and transcription factors (Casadio et al., 2013; Herglotz et al., 2013; Hyllus et al., 2007; Waldmann et al., 2011). Additionally, non-catalytic functions of PRMT6 and indirect mechanisms might account for transcriptional deregulation of these H3R2me2a-independent target genes. For example, *CDKN1A*, which has been shown to be a direct target of H3R2me2a in several human cell lines (Kleinschmidt et al., 2012; Phalke et al., 2012; Stein et al., 2012), does not show any enrichment of the mark in its promoter or enhancer region in NT2/D1 cells, despite being upregulated in the absence of PRMT6 (data not shown). Interestingly, the transcription factor MTF, which has been reported to activate *CDKN1A* expression (Carreira et al., 2005), is a downregulated and direct H3R2me2a target gene in NT2/D1 cells and hence might be responsible for the enhanced *CDKN1A* transcript levels in PRMT6 knockout cells.

Our analysis of the gene-regulatory role of H3R2me2a at promoter and enhancer sites uncovered further unexpected insights. This mark seems to execute opposing transcriptional effects depending on its genomic location: repressive functions at promoters and activating functions at enhancers (Figure 7). Promoter-bound H3R2me2a co-localizes with high H3K4me3 occupancy and antagonizes the deposition of this well-known active promoter mark, likely by interfering with the recruitment of KMT2A. This results in a diminished transcriptional activity of target genes. Our findings extend the understanding on the previously reported repressive nature of H3R2me2a, since this rather occurs at active genes than at silent gene loci, causing a restraint of their transcriptional output (Guccione et al., 2007; Hyllus et al., 2007; Iberg et al., 2008). PRMT6, potentially via H3R2me2a deposition at gene promoters, leads to fine-tuning of the transcriptional program in NT2/D1 cells and impedes unauthorized high expression of pluripotency genes as well as differentiation-associated genes (Figure 7A). In contrast, non-promoter H3R2me2a peaks co-localize with active enhancer marks, such as H3K4me1 and H3K27ac. Here, H3R2me2a might positively influence the deposition of these two enhancer marks, possibly by recruitment of KMT2D (subsequently p300), and thereby contributes to transcriptional activation of the associated genes (Figure 7B). At both locations, promoter as well as enhancer sites, H3R2me2a seems to modulate the deposition of adjacent histone marks, in agreement with the concept that arginine methylation exerts its regulatory activity by facilitating or diminishing protein-protein interactions. Whether H3R2me2a is sufficient and thereby decisive for regulating the chromatin recruitment of KMT2A and KMT2D requires further investigations in the future. Collectively, we conclude that PRMT6, likely via its catalytic activity and H3R2me2a, regulates the



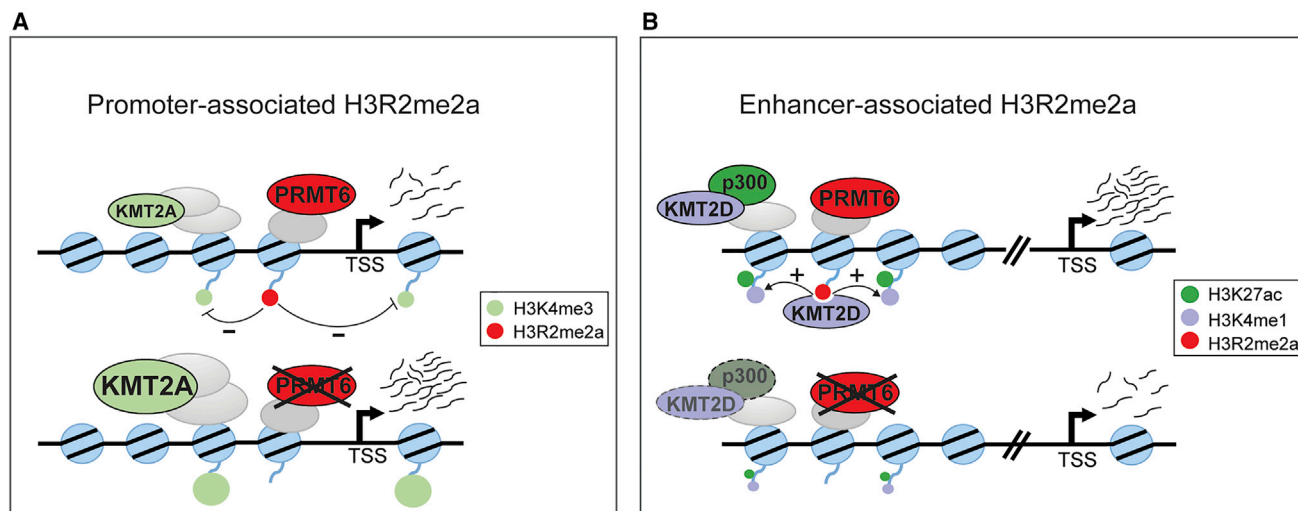


**Figure 7. Model for the PRMT6-Dependent Deposition and Function of H3R2me2a at Promoter and Enhancer Sites**

(A) Promoter-deposited H3R2me2a peaks (red circles) occur in proximity to the TSS of target genes, which are concomitantly marked with high H3K4me3 occupancy (green circles). These H3R2me2a binding sites associate with genes of medium to high expression levels. Here, PRMT6, potentially via H3R2me2a, diminishes the transcriptional output of target genes by counteracting KMT2A/H3K4me3 (upper panel). Deletion of PRMT6 and concomitant loss of H3R2me2a lead to increased binding of KMT2A as well as increased occupancy of H3K4me3 (as illustrated by the larger green circles) and unauthorized high expression of pluripotency and differentiation-associated genes (lower panel).

(B) Enhancer-deposited H3R2me2a (red circles) co-localizes with the active enhancer marks H3K4me1 and H3K27ac (purple and green circles, respectively). Here, PRMT6, potentially via H3R2me2a, enhances the transcriptional output of target genes by positively influencing the deposition of H3K4me1/H3K27ac, possibly through recruitment of KMT2D and subsequently p300 (upper panel). Deletion of PRMT6 and concomitant loss of H3R2me2a coincide with decreased binding of KMT2D as well as occupancy of H3K4me1/H3K27ac (as illustrated by the smaller circles) and impaired differentiation-dependent transcriptional activation of these important target genes (lower panel).

transcriptional output of genes relevant for neural differentiation through opposing effects on promoter and enhancer activities (Figure 7).

## EXPERIMENTAL PROCEDURES

### Cell Lines and Reagents

NT2/D1, U2OS, HeLa, and HEK293T cells were maintained in DMEM supplemented with 10% fetal calf serum (FCS) (Gibco-BRL) and 1% penicillin/streptomycin at 37°C and 5% CO<sub>2</sub>. Neural differentiation of NT2/D1 cells was induced with 1 μM ATRA (Sigma) according to the protocol of Andrews (1984). MS049 hydrochloride was purchased from Sigma (SML15530). Detailed information on antibodies and plasmids is supplied in Supplemental Experimental Procedures.

### Production of Lentiviral Particles and Infection of Cells

For CRISPR/Cas9-mediated deletion of *PRMT6* in NT2/D1 and U2OS cell as well as doxycycline-inducible expression of *PRMT6* in NT2/D1 KO cells, HEK293T cells were transfected with packaging plasmids and lentiviral expression plasmids. Subsequently, lentiviral particles were used for cell infection as described in Supplemental Experimental Procedures.

### Synthetic Histone Peptides

Unmodified and modified N-terminal histone peptides followed by a C-terminal cysteine residue or biotin moiety were obtained from Peptide Specialty Laboratories (Heidelberg, Germany). Modified peptides were synthesized by using either monomethylated, asymmetrically dimethylated, symmetrically dimethylated arginine, or mono-, di-, trimethylated lysine. Dot blot analysis and peptide pull-downs were performed as described in Supplemental Experimental Procedures.

### Flow Cytometry

For quantification of the cell cycle distribution as well as pluripotency marker analysis, flow cytometry was used as described in Supplemental Experimental Procedures.

### Animals

Constitutive *Prmt6*<sup>−/−</sup> (KO) mice were provided by the laboratory of Stephane Richards (Neault et al., 2012). For generation of *Prmt6*<sup>+/−</sup> (KO), *Prmt6*<sup>+/−</sup> (HET), and *Prmt6*<sup>+/+</sup> (WT) embryos of E12.5, pregnant female mice (*Prmt6* HET) were sacrificed by cervical dislocation, and embryos were decapitated. Killing of mice for tissue preparation was as approved by the animal protection commissioner of the University of Marburg. Tissue preparation and analysis are described in detail in Supplemental Experimental Procedures.

### RNA Isolation, RT-qPCR, and RNA-Seq

RT-qPCR and RNA-seq were performed as described in Supplemental Experimental Procedures.

### ChIP-qPCR and ChIP-Seq

For immunoprecipitation of histone marks, cells were cross-linked with 1% formaldehyde, whereas for immunoprecipitation of histone modifiers additionally disuccinimidyl glutarate (DSG) was used. ChIP experiments and detailed settings of genomic analyses are described in Supplemental Experimental Procedures.

### Statistical Analysis

All experiments were performed at least three times (biological replicates). Reproducible and representative datasets are shown. Corresponding statistical tests are mentioned in the figure legends. Error bars represent mean ± SD of triplicate measurements.

## DATA AND SOFTWARE AVAILABILITY

The accession number for the ChIP-seq and RNA-seq data reported in this paper is GEO: GSE107612.

## SUPPLEMENTAL INFORMATION

Supplemental Information includes Supplemental Experimental Procedures and eight figures and can be found with this article online at <https://doi.org/10.1016/j.celrep.2018.08.052>.

## ACKNOWLEDGMENTS

We thank all members of the U.-M.B. laboratory for their support during the work progress and Inge Sprenger and Christiane Rohrbach for technical assistance. We are grateful to Sophie Meyer and Felix Schneider for their support in murine brain analyses. We thank Stéphane Richard for providing the *Prmt6*<sup>−/−</sup> mouse model to us. This work was funded by DFG (Deutsche Forschungsgemeinschaft) Grants TRR81 A03, SFB1213 A05, BA 2292/1, and BA 2292/4 (to U.-M.B.) and GRK1213 and RU 1232/7-1 (to M.B.R.) and by Deutsche José Carreras Leukämie-Stiftung e.V. Grant DJCLS R 13/17 (to U.-M.B.).

## AUTHORS CONTRIBUTIONS

C.B., P.S., M.M., R.R.N., G.H.-S., and A.N. performed experiments. E.K., R.F., and S.S.P. generated reagents. C.B., P.S., M.M., M.B.R., G.H.-S., F.F., M.B., T.S., S.P., and U.-M.B. analyzed data. U.-M.B. supervised. C.B. and U.-M.B. wrote the paper.

## DECLARATION OF INTERESTS

The authors declare no competing interests.

Received: December 28, 2017

Revised: July 19, 2018

Accepted: August 17, 2018

Published: September 18, 2018

## REFERENCES

- Andrews, P.W. (1984). Retinoic acid induces neuronal differentiation of a cloned human embryonal carcinoma cell line in vitro. *Dev. Biol.* 103, 285–293.
- Barski, A., Cuddapah, S., Cui, K., Roh, T.Y., Schones, D.E., Wang, Z., Wei, G., Chepelev, I., and Zhao, K. (2007). High-resolution profiling of histone methylations in the human genome. *Cell* 129, 823–837.
- Calo, E., and Wysocka, J. (2013). Modification of enhancer chromatin: what, how, and why? *Mol. Cell* 49, 825–837.
- Carreira, S., Goodall, J., Aksan, I., La Rocca, S.A., Galibert, M.D., Denat, L., Larue, L., and Goding, C.R. (2005). Mitf cooperates with Rb1 and activates p21Cip1 expression to regulate cell cycle progression. *Nature* 433, 764–769.
- Casadio, F., Lu, X., Pollock, S.B., LeRoy, G., Garcia, B.A., Muir, T.W., Roeder, R.G., and Allis, C.D. (2013). H3R42me2a is a histone modification with positive transcriptional effects. *Proc. Natl. Acad. Sci. USA* 110, 14894–14899.
- Damez-Werno, D.M., Sun, H., Scobie, K.N., Shao, N., Rabkin, J., Dias, C., Calipari, E.S., Maze, I., Pena, C.J., Walker, D.M., et al. (2016). Histone arginine methylation in cocaine action in the nucleus accumbens. *Proc. Natl. Acad. Sci. USA* 113, 9623–9628.
- Dhar, S.S., Lee, S.H., Kan, P.Y., Voigt, P., Ma, L., Shi, X., Reinberg, D., and Lee, M.G. (2012). Trans-tail regulation of MLL4-catalyzed H3K4 methylation by H4R3 symmetric dimethylation is mediated by a tandem PHD of MLL4. *Genes Dev.* 26, 2749–2762.
- Dhawan, S., Georgia, S., Tschen, S.I., Fan, G., and Bhushan, A. (2011). Pancreatic  $\beta$  cell identity is maintained by DNA methylation-mediated repression of *Arx*. *Dev. Cell* 20, 419–429.
- Gayatri, S., and Bedford, M.T. (2014). Readers of histone methylarginine marks. *Biochim. Biophys. Acta* 1839, 702–710.
- Glauche, I., Moore, K., Thielecke, L., Horn, K., Loeffler, M., and Roeder, I. (2009). Stem cell proliferation and quiescence—two sides of the same coin. *PLoS Comput. Biol.* 5, e1000447.
- Guccione, E., Bassi, C., Casadio, F., Martinato, F., Cesaroni, M., Schuchlantz, H., Lüscher, B., and Amati, B. (2007). Methylation of histone H3R2 by PRMT6 and H3K4 by an MLL complex are mutually exclusive. *Nature* 449, 933–937.
- Harrison, M.J., Tang, Y.H., and Dowhan, D.H. (2010). Protein arginine methyltransferase 6 regulates multiple aspects of gene expression. *Nucleic Acids Res.* 38, 2201–2216.
- Herglotz, J., Kuvardina, O.N., Kolodziej, S., Kumar, A., Hussong, H., Grez, M., and Lausen, J. (2013). Histone arginine methylation keeps RUNX1 target genes in an intermediate state. *Oncogene* 32, 2565–2575.
- Houldsworth, J., Heath, S.C., Bosl, G.J., Studer, L., and Chaganti, R.S.K. (2002). Expression profiling of lineage differentiation in pluripotent human embryonal carcinoma cells. *Cell Growth Differ.* 13, 257–264.
- Hyllus, D., Stein, C., Schnabel, K., Schiltz, E., Imhof, A., Dou, Y., Hsieh, J., and Bauer, U.-M. (2007). PRMT6-mediated methylation of R2 in histone H3 antagonizes H3 K4 trimethylation. *Genes Dev.* 21, 3369–3380.
- Iberg, A.N., Espejo, A., Cheng, D., Kim, D., Michaud-Levesque, J., Richard, S., and Bedford, M.T. (2008). Arginine methylation of the histone H3 tail impedes effector binding. *J. Biol. Chem.* 283, 3006–3010.
- Kirmizis, A., Santos-Rosa, H., Penkett, C.J., Singer, M.A., Vermeulen, M., Mann, M., Bähler, J., Green, R.D., and Kouzarides, T. (2007). Arginine methylation at histone H3R2 controls deposition of H3K4 trimethylation. *Nature* 449, 928–932.
- Kleinschmidt, M.A., de Graaf, P., van Teeffelen, H.A., and Timmers, H.T. (2012). Cell cycle regulation by the PRMT6 arginine methyltransferase through repression of cyclin-dependent kinase inhibitors. *PLoS One* 7, e41446.
- Lee, V.M., and Andrews, P.W. (1986). Differentiation of NTERA-2 clonal human embryonal carcinoma cells into neurons involves the induction of all three neurofilament proteins. *J. Neurosci.* 6, 514–521.
- Lee, Y.H., Ma, H., Tan, T.Z., Ng, S.S., Soong, R., Mori, S., Fu, X.Y., Zernicka-Goetz, M., and Wu, Q. (2012). Protein arginine methyltransferase 6 regulates embryonic stem cell identity. *Stem Cells Dev.* 21, 2613–2622.
- McKee, A.E., Minet, E., Stern, C., Riahi, S., Stiles, C.D., and Silver, P.A. (2005). A genome-wide in situ hybridization map of RNA-binding proteins reveals anatomically restricted expression in the developing mouse brain. *BMC Dev. Biol.* 5, 14.
- Michaud-Levesque, J., and Richard, S. (2009). Thrombospondin-1 is a transcriptional repression target of PRMT6. *J. Biol. Chem.* 284, 21338–21346.
- Neault, M., Mallette, F.A., Vogel, G., Michaud-Levesque, J., and Richard, S. (2012). Ablation of PRMT6 reveals a role as a negative transcriptional regulator of the p53 tumor suppressor. *Nucleic Acids Res.* 40, 9513–9521.
- Phalke, S., Mzoughi, S., Bezzi, M., Jennifer, N., Mok, W.C., Low, D.H., Thike, A.A., Kuznetsov, V.A., Tan, P.H., Voorhoeve, P.M., and Guccione, E. (2012). p53-Independent regulation of p21Waf1/Cip1 expression and senescence by PRMT6. *Nucleic Acids Res.* 40, 9534–9542.
- Rosenfeld, J.A., Wang, Z., Schones, D.E., Zhao, K., DeSalle, R., and Zhang, M.Q. (2009). Determination of enriched histone modifications in non-genic portions of the human genome. *BMC Genomics* 10, 143.
- Shen, Y., Szweczyk, M.M., Eram, M.S., Smil, D., Kaniskan, H.Ü., de Freitas, R.F., Senisterra, G., Li, F., Schapira, M., Brown, P.J., et al. (2016). Discovery of a potent, selective, and cell-active dual inhibitor of protein arginine methyltransferase 4 and protein arginine methyltransferase 6. *J. Med. Chem.* 59, 9124–9139.
- Stein, C., Riedl, S., Rüttnick, D., Nötzel, R.R., and Bauer, U.M. (2012). The arginine methyltransferase PRMT6 regulates cell proliferation and senescence through transcriptional repression of tumor suppressor genes. *Nucleic Acids Res.* 40, 9522–9533.

- Stein, C., Nötzold, R.R., Riedl, S., Bouchard, C., and Bauer, U.M. (2016). The arginine methyltransferase PRMT6 cooperates with polycomb proteins in regulating HOXA gene expression. *PLoS One* *11*, e0148892.
- Torres-Padilla, M.E., Parfitt, D.E., Kouzarides, T., and Zernicka-Goetz, M. (2007). Histone arginine methylation regulates pluripotency in the early mouse embryo. *Nature* *445*, 214–218.
- Waldmann, T., Izzo, A., Kamieniarz, K., Richter, F., Vogler, C., Sarg, B., Lindner, H., Young, N.L., Mittler, G., Garcia, B.A., and Schneider, R. (2011). Methylation of H2AR29 is a novel repressive PRMT6 target. *Epigenetics Chromatin* *4*, 11.
- Wang, C., Lee, J.-E., Lai, B., Macfarlan, T.S., Xu, S., Zhuang, L., Liu, C., Peng, W., and Ge, K. (2016). Enhancer priming by H3K4 methyltransferase MLL4 controls cell fate transition. *Proc. Natl. Acad. Sci. USA* *113*, 11871–11876.
- Wang, S.P., Tang, Z., Chen, C.W., Shimada, M., Koche, R.P., Wang, L.H., Nakadal, T., Chramiec, A., Krivtsov, A.V., Armstrong, S.A., and Roeder, R.G. (2017). A UTX-MLL4-p300 transcriptional regulatory network coordinately shapes active enhancer landscapes for eliciting transcription. *Mol. Cell* *67*, 308–321.e6.
- Yang, Y., and Bedford, M.T. (2013). Protein arginine methyltransferases and cancer. *Nat. Rev. Cancer* *13*, 37–50.

**Supplemental Information**

**Genomic Location of PRMT6-Dependent  
H3R2 Methylation Is Linked  
to the Transcriptional Outcome of Associated Genes**

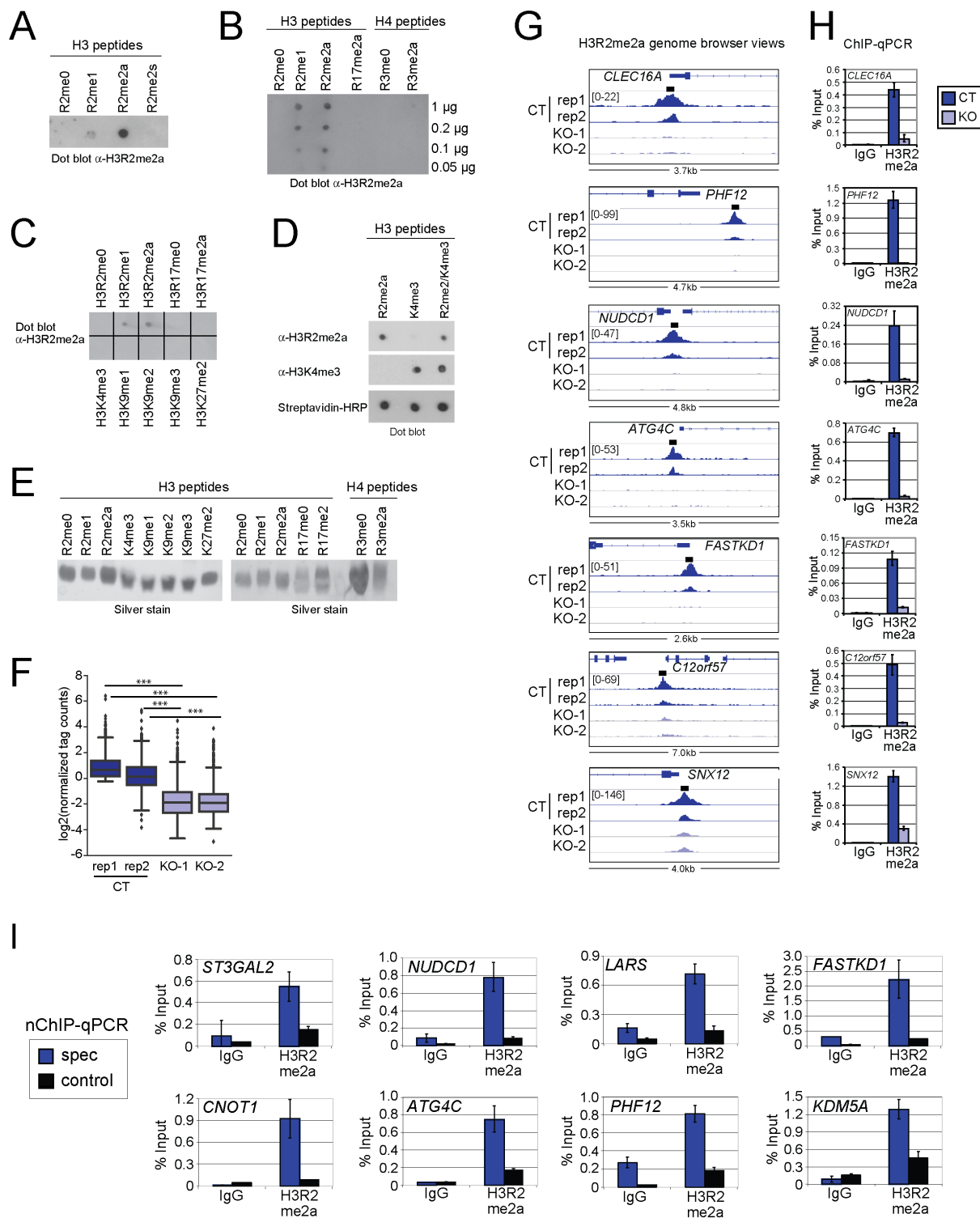
**Caroline Bouchard, Peeyush Sahu, Marion Meixner, René Reiner Nötzold, Marco B. Rust, Elisabeth Kremmer, Regina Feederle, Gene Hart-Smith, Florian Finkernagel, Marek Bartkuhn, Soni Savai Pullamsetti, Andrea Nist, Thorsten Stiewe, Sjaak Philipsen, and Uta-Maria Bauer**



## Supplemental Information

### Supplemental Figures and Legends

## Suppl. Figure S1



### Suppl.Figure S1

**Characterization of the  $\alpha$ -H3R2me2a rat monoclonal antibody by dot blot analyses (A-E) and additional validations of H3R2me2a binding sites in undifferentiated NT2/D1 cells (F-I). Related to Figure 1.**

**A:** H3 peptides (aa 1-8, 1 $\mu$ g each) either unmodified at R2 (R2me0), monomethylated (R2me1), asymmetrically dimethylated (R2me2a) or symmetrically dimethylated (R2me2s) were spotted on nitrocellulose and stained with rat monoclonal  $\alpha$ -H3R2me2a.

**B:** Indicated amounts of H3 peptides (aa 1-30 or 1-24) and H4 peptides (aa 1-15) either unmodified or modified were spotted on nitrocellulose and stained with rat monoclonal  $\alpha$ -H3R2me2a.

**C:** Various H3 peptides (1 $\mu$ g each) either unmodified or modified were spotted on nitrocellulose and stained with rat monoclonal  $\alpha$ -H3R2me2a.

**D:** H3 peptides (aa 1-15 and biotinylated at the C-terminus, 1 $\mu$ g each) modified at R2me2a, K4me3 or double modified (R2me2a/K4me3) were spotted on nitrocellulose and stained with the indicated antibodies or as loading control with streptavidin-HRP (Invitrogen).

**E:** The various H3 and H4 peptides (1 $\mu$ g each, used in A-D) were visualized by SDS-PAGE and silver staining.

**F:** Boxplot analysis illustrates the normalized H3R2me2a tag counts of NT2/D1 CT (two ChIP-seq replicates) and both NT2D1 KO cell lines. \*\*\*:  $p \leq 0.001$  using Welch's t-test.

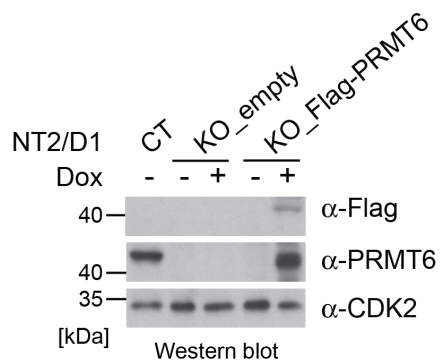
**G:** Genome browser views of the H3R2me2a ChIP-seq data sets of NT2/D1 CT (two replicates) and both KO cell lines depicted for additional gene loci. Positions of amplicons generated by qPCR are depicted as black boxes above the top browser tracks. Data range is indicated in brackets.

**H:** ChIP-qPCR assays were performed in NT2/D1 CT and KO cells (= KO-2, which we employed in all subsequent experiments as PRMT6 knockout cell line) using control antibodies (IgG) and  $\alpha$ -H3R2me2a with primers amplifying the H3R2me2a peaks of the depicted loci (in G). Recruitment is displayed in % input of chromatin (mean  $\pm$  SD of triplicates).

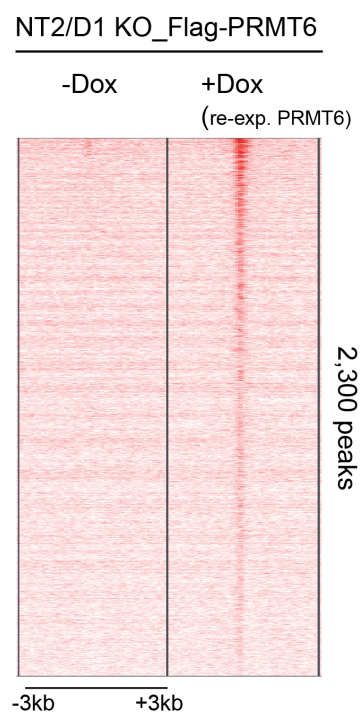
**I:** Native (unfixed) chromatin was isolated from NT2/D1 cells and digested using Micrococcal nuclease (as described in Umlauf et al., 2005). Mononucleosomes were employed in native ChIP (nChIP) experiments using control antibodies (IgG) and  $\alpha$ -H3R2me2a. Subsequently, qPCR assays were performed with primers amplifying either the H3R2me2a peaks (spec) or a nearby control region (control) of the indicated loci. Positions of amplicons generated by qPCR (spec) are depicted in Fig. 1D and S1G. Recruitment is displayed in % input of chromatin (mean  $\pm$  SD of triplicates).

# Suppl. Figure S2

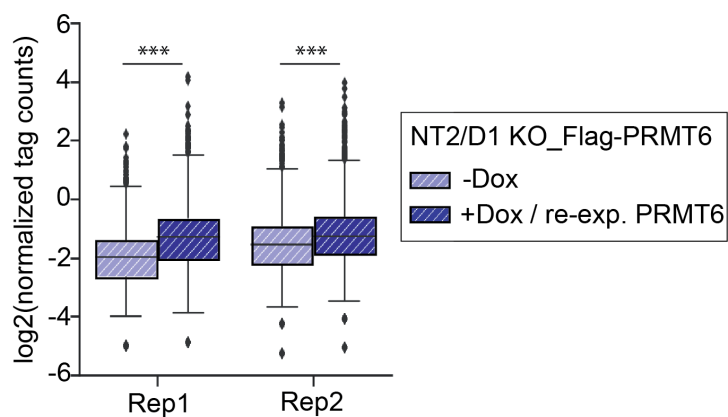
**A**



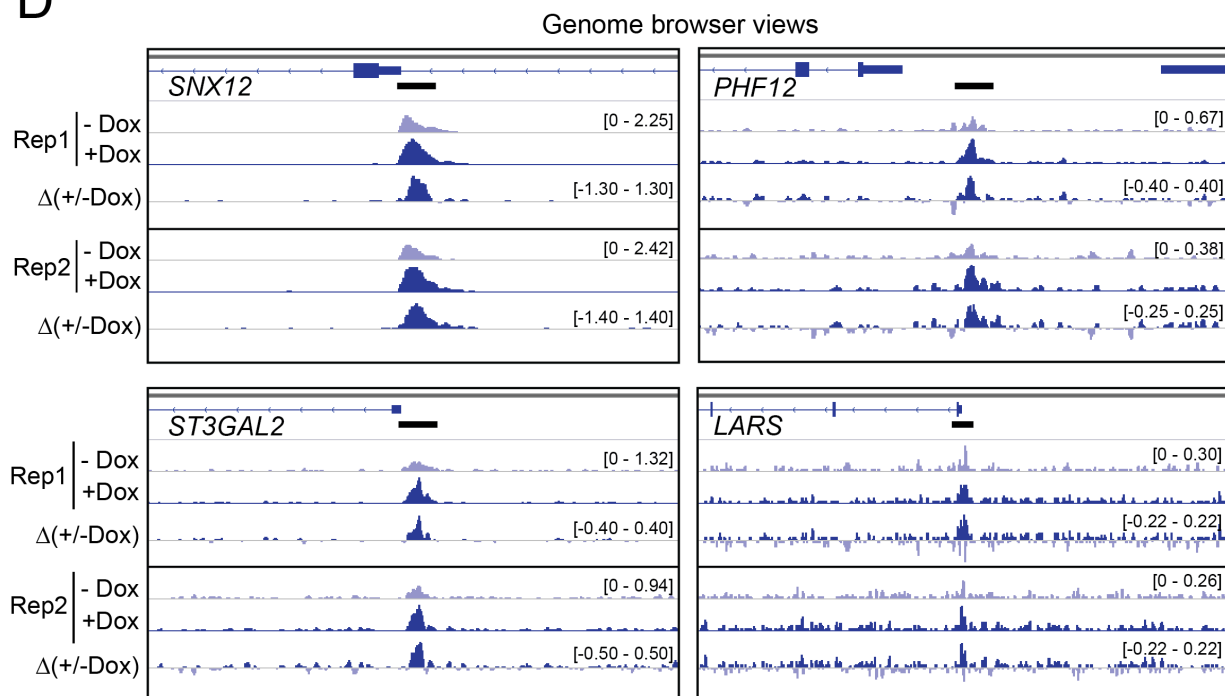
**B**



**C**



**D**



### Suppl.Figure S2

#### Re-expression of PRMT6 in NT2/D1 KO cells and H3R2me2a ChIP-seq analysis. Related to Figure 1.

**A:** Protein extracts of NT2/D1 CT cells and KO cells either infected with pInducer20 empty vector or pInducer20-3xFlag-PRMT6 (-/+ doxycycline for 6 days) were analyzed by Western blot using the indicated antibodies ( $\alpha$ -Flag,  $\alpha$ -PRMT6,  $\alpha$ -CDK2) to monitor doxycycline-inducible expression of Flag-PRMT6 in NT2/D1 KO\_Flag-PRMT6 cells. CDK2 staining served as loading control. Size markers (in kDa) are shown on the left.

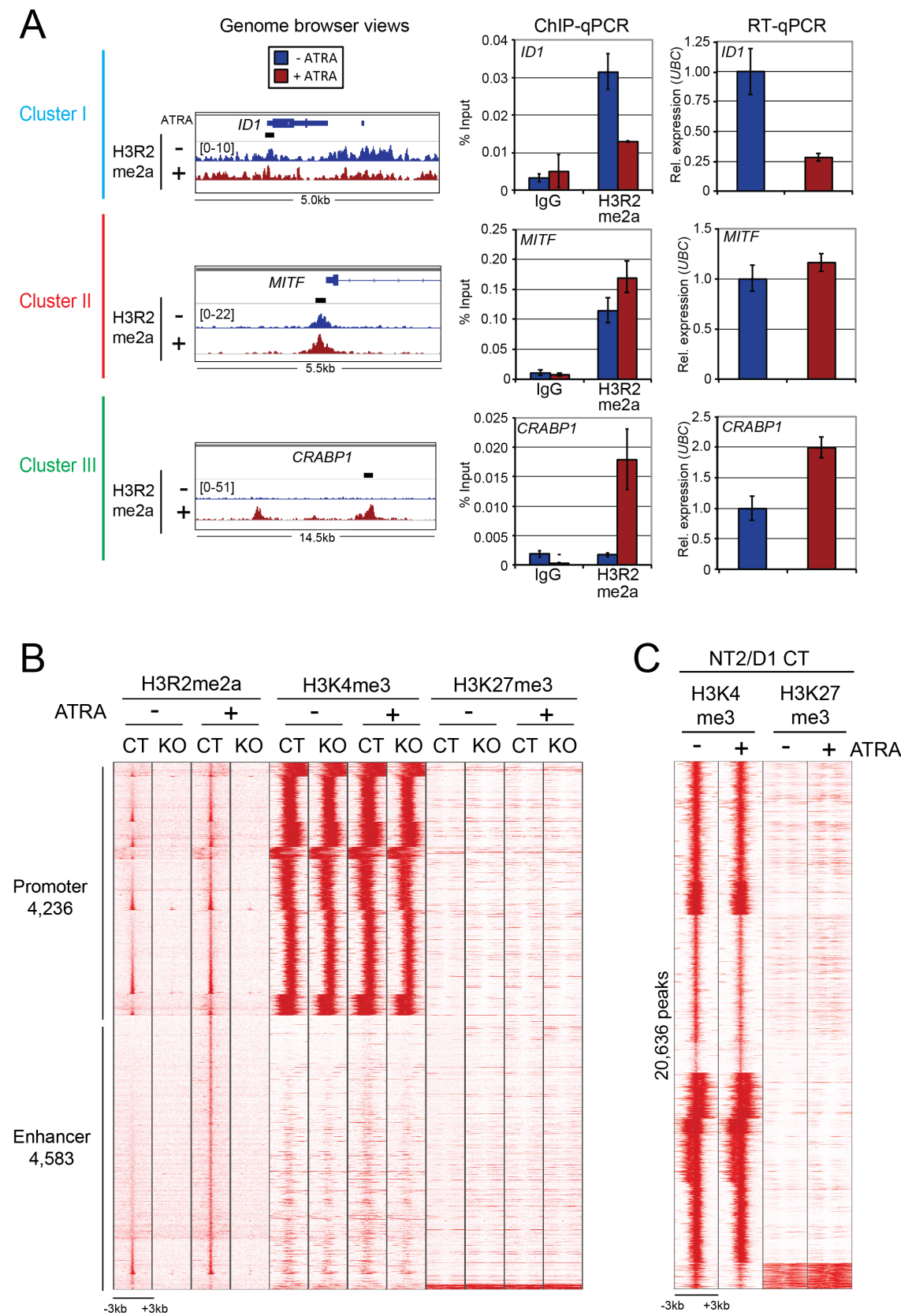
**B:** Heatmap displays the H3R2me2a ChIP-seq signals (replicate 1) in NT2/D1 KO\_Flag-PRMT6 cells +/- doxycycline over the 2,300 binding sites sorted in the descending order of their signal strength (+/- 3kb around the centered summits).

**C:** Boxplot analysis illustrates the normalized H3R2me2a tag counts (of two ChIP-seq replicates) in NT2D1 KO\_Flag-PRMT6 cells in the absence (- doxycycline) or presence (+ doxycycline) of PRMT6 re-expression. \*\*\*:  $p \leq 0.001$  using Welch's t-test.

**D:** Genome browser views of the H3R2me2a ChIP-seq data sets in NT2/D1 KO\_Flag-PRMT6 cells (of replicates 1 and 2) +/- doxycycline are depicted for four gene loci. H3R2me2a signal differences between +/- doxycycline ( $\Delta$ +/- Dox) are illustrated in a separate track for each replicate. Positions of H3R2me2a peaks, which show an increased H3R2me2a occupancy upon Flag-PRMT6 expression (+ doxycycline), are highlighted with black boxes above the top browser tracks. Normalized data range is indicated in brackets.



Suppl.Figure S3



### Suppl.Figure S3

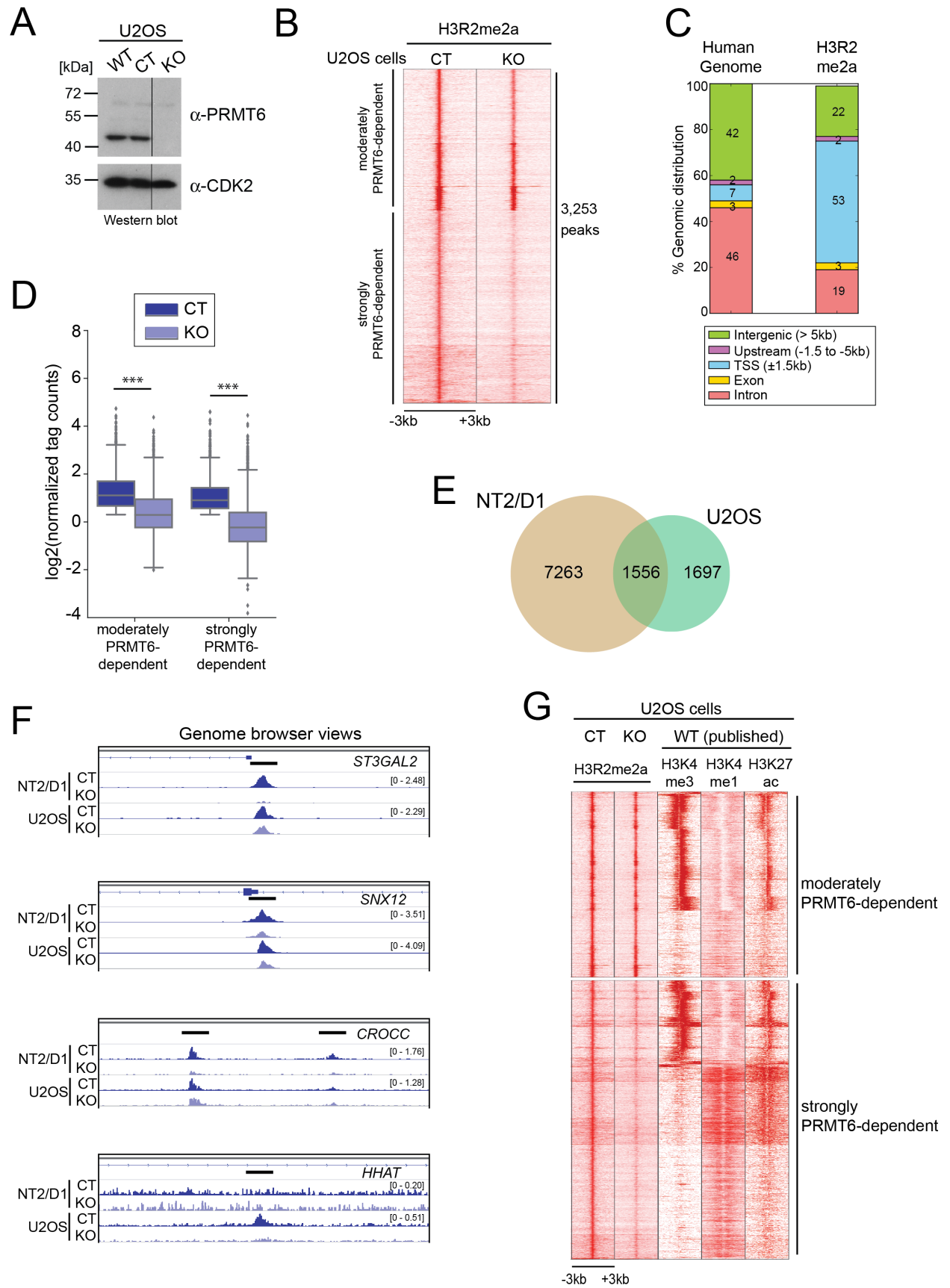
**Additional validations of H3R2me2a binding sites for all three clusters in NT2/D1 CT cells (A) and analysis of a potential bivalency (H3K4me3/H3K27me3 co-occupancy) of H3R2me2a peaks (B, C). Related to Figure 2.**

**A:** Genome browser views of the H3R2me2a ChIP-seq data sets of NT2/D1 CT cells +/- ATRA are depicted for gene loci illustrating the three clusters (left panels): *IDI* (cluster I), *MITF* (cluster II) and *CRABP1* (cluster III) (left panels). Positions of amplicons generated by qPCR are depicted as black boxes above the top browser tracks. Data range is indicated in brackets. ChIP-qPCR assays were performed using control antibodies (IgG) and  $\alpha$ -H3R2me2a and primers amplifying the H3R2me2a peaks of the depicted loci. Recruitment is displayed in % input of chromatin, mean  $\pm$  SD of triplicates (middle panels). Total RNA was analyzed by RT-qPCR for the transcript levels derived from these three gene loci. Values were normalized to *UBIQUITIN* (*UBC*) expression and presented relative to the - ATRA condition, mean  $\pm$  SD of triplicates (right panels).

**B:** Heatmap illustrates the H3R2me2a ChIP signals over 8,819 sites in comparison to the ChIP-seq profile of H3K4me3 and H3K27me3 in NT2/D1 CT and KO cells +/- ATRA with regions classified in promoters (4,236 sites displaying high H3K4me3 occupancy, as shown in Fig. 2D) or enhancers (4,583 sites displaying high H3K4me1/H3K27ac occupancy, as shown in Fig. 2D).

**C:** Heatmap illustrates the H3K4me3 ChIP signals for all 20,636 H3K4me3 peaks in comparison to the H3K27me3 ChIP-seq in NT2/D1 CT cells +/- ATRA, confirming the presence of bivalent loci in NT2/D1 cells, which do not overlap with H3R2me2a sites (as shown in B).

# Suppl. Figure S4



#### Suppl.Figure S4

##### H3R2me2a ChIP-seq analysis in U2OS cells. Related to Figure 2.

**A:** Protein extracts of U2OS either wild type (WT), *GFP* control gRNA infected (CT) or *PRMT6* gRNAs infected (KO) were analyzed by Western blot using the indicated antibodies ( $\alpha$ -PRMT6,  $\alpha$ -CDK2) to monitor *PRMT6* knockout in the U2OS KO cell clone. CDK2 staining served as loading control. Size markers (in kDa) are shown on the left.

**B:** Heatmap displays the H3R2me2a ChIP-seq signals in U2OS CT and KO cells over the 3,253 binding sites sorted in moderate and strong PRMT6-dependency (+/- 3kb around the centered summits).

**C:** Relative distribution of the 3,253 H3R2me2a peaks in U2OS cells (of B) is shown within different genomic regions compared to the distribution of these regions in the human genome.

**D:** Boxplot analysis illustrates the normalized H3R2me2a tag counts of the ChIP-seq analyses (in B) for moderately and strongly PRMT6-dependent peaks in U2OS CT and KO cells. \*\*\*:  $p \leq 0.001$  using Welch's t-test.

**E:** Venn diagram illustrates the overlap of H3R2me2a binding sites gained from ChIP-seq in NT2/D1 CT and U2OS CT cells.

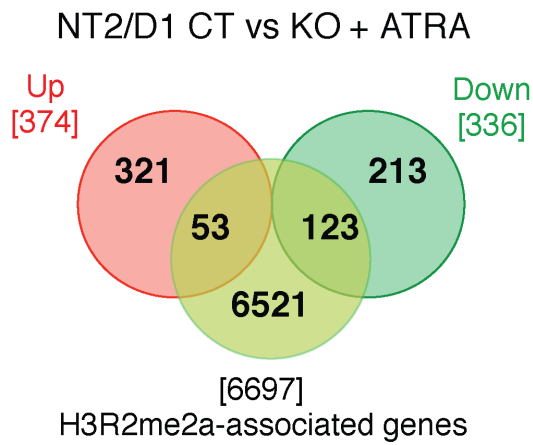
**F:** Genome browser views of the H3R2me2a ChIP-seq data sets of NT2/D1 CT / KO and U2OS CT / KO cells are depicted for four gene loci. Positions of H3R2me2a peaks, which show a decreased H3R2me2a occupancy upon PRMT6 deletion, are highlighted with black boxes above the top browser tracks. Normalized data range is indicated in brackets. *ST3GAL2*, *SNX12* and *CROCC* represent gene loci with common H3R2me2a peaks in both cell lines. *HHAT* represents a gene locus with a H3R2me2a peak specific for U2OS cells.

**G:** Heatmap illustrates the H3R2me2a ChIP signals of U2OS CT cells over 3,253 sites in comparison to published ChIP-seq profiles of H3K4me3, H3K4me1 and H3K27ac of U2OS wild type cells (WT) classified in moderately and strongly PRMT6-dependent peaks (as shown in B).

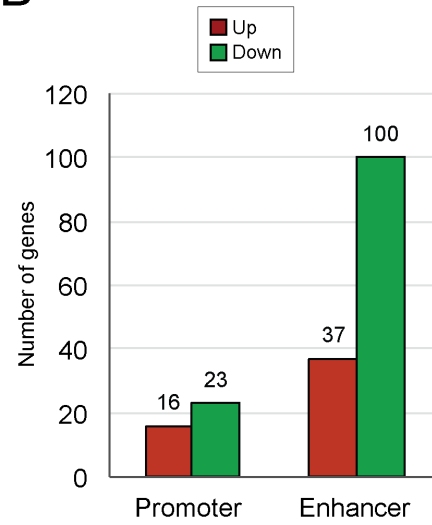


# Suppl.Figure S5

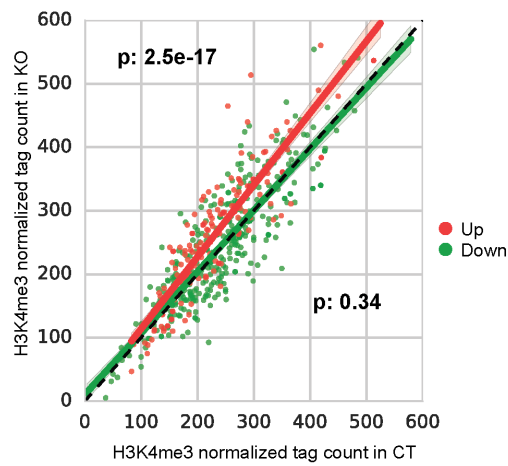
A



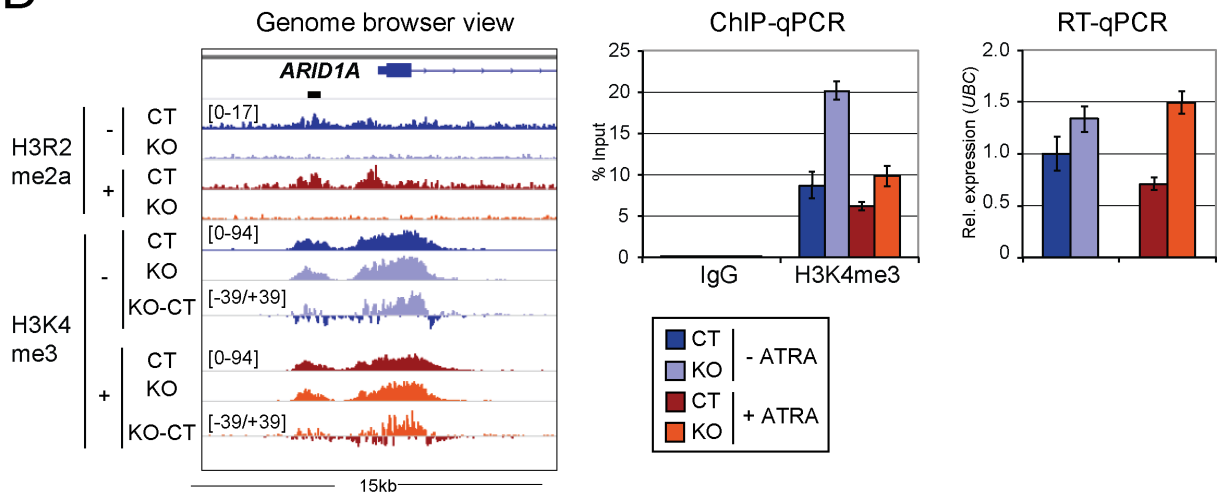
B



C



D



**Suppl.Figure S5**

**RNA-seq analysis of NT2/D1 CT and KO cells + ATRA (A, B) and influence of PRMT6 knockout on H3K4me3 deposition in NT2/D1 cells (C, D). Related to Figures 2 and 3.**

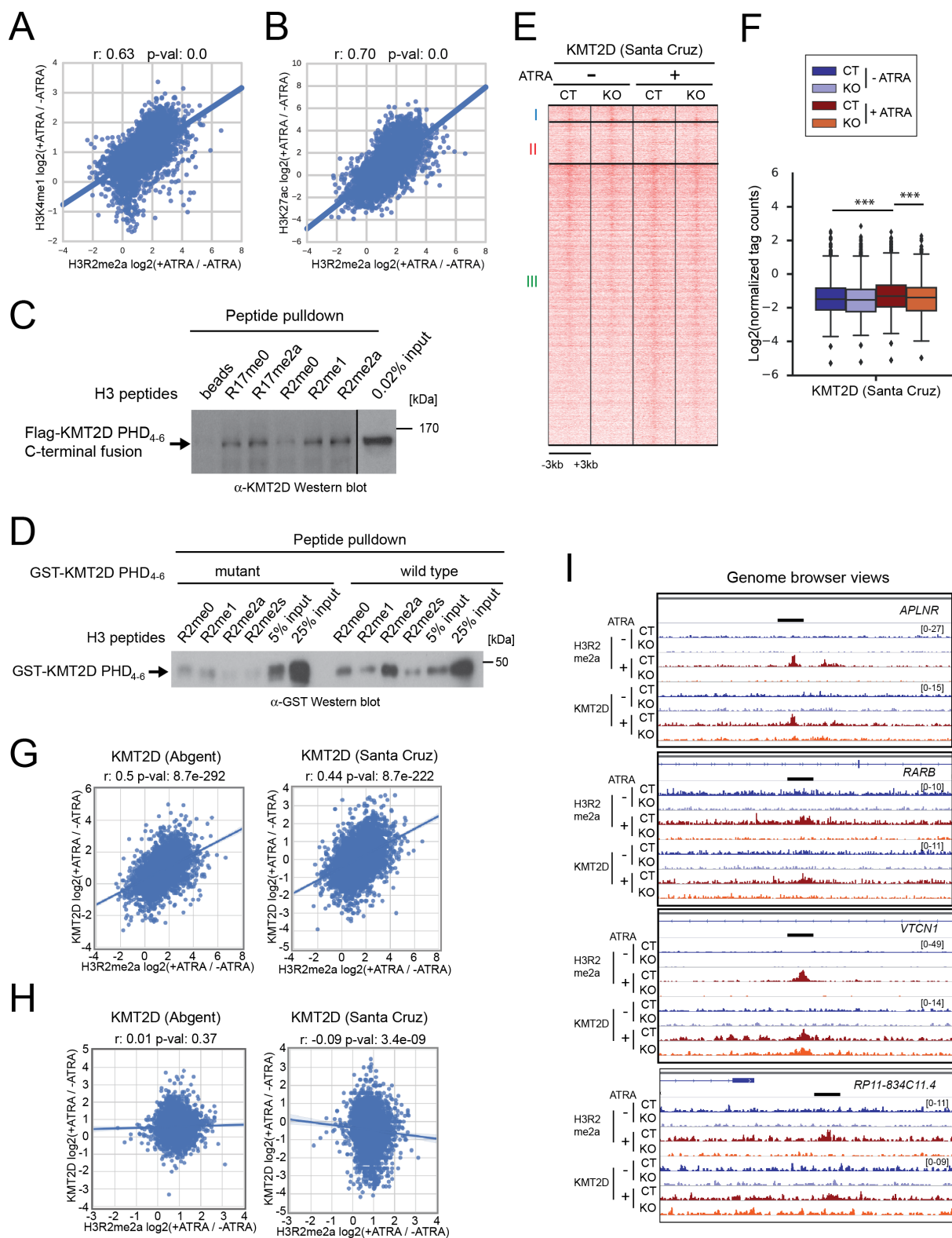
**A:** Venn diagram shows the intersection of differentially expressed genes upon PRMT6 deletion separated in up- and down-regulated genes and genes associated with H3R2me2a binding sites in NT2/D1 CT cells + ATRA.

**B:** Expression changes in NT2/D1 cells + ATRA upon PRMT6 knockout (at least fold change  $\pm 2$  and  $FDR \leq 0.01$ ) are depicted in gene numbers for either promoter-associated or enhancer-associated H3R2me2a binding sites.

**C:** Scatter plot presents the normalized H3K4me3 tag counts for up- (red fitted regression line) and down-regulated (green fitted regression line) genes in NT2/D1 CT versus KO cells. Black dotted diagonal indicates identical levels of the H3K4me3 marks in both cell lines. P-values are depicted (Welch's t-test).

**D:** Genome browser views of the H3R2me2a and H3K4me3 ChIP-seq data sets generated in NT2/D1 CT and KO cells +/- ATRA are shown for the cluster III gene *ARID1A* (left panel). H3K4me3 signal differences between NT2/D1 KO and CT are illustrated in separate tracks (KO-CT). Position of amplicon generated by qPCR is depicted as a black box above the browser track. Data range is indicated in brackets. ChIP-qPCR assays were performed using control antibodies (IgG) and  $\alpha$ -H3K4me3 and primers encompassing the H3R2me2a peak of *ARID1A*. Recruitment is displayed in % input of chromatin, mean  $\pm$  SD of triplicates (middle panel). Total RNA was analyzed by RT-qPCR for transcript levels of *ARID1A*. Values were normalized to *UBIQUITIN (UBC)* expression and presented relative to NT2/D1 CT cells -ATRA, mean  $\pm$  SD of triplicates (right panel).

# Suppl.Figure S6



### Suppl.Figure S6

#### Cross-talk between H3R2me2a and the enhancer marks H3K4me1/H3K27ac as well as KMT2D. Related to Figure 4.

**A, B:** Fold change of H3R2me2a levels in NT2/D1 cells  $\pm$  ATRA was plotted versus fold change of H3K4me1 (in A) or H3K27ac (in B) levels for all enhancer peaks. The Spearman correlation coefficient  $r$  and the  $p$ -val are indicated.

**C:** Indicated histone H3 peptides (aa 1-24 for peptides encompassing R17 and aa 1-30 for peptides encompassing R2) were covalently coupled to Sulfolink-beads and incubated with HeLa cell extract overexpressing Flag-KMT2D PHD<sub>4-6</sub> C-terminal fusion protein (Dhar et al., 2012). Pulldown reactions and 0.02% input of cell extract were resolved by SDS-PAGE and analyzed by  $\alpha$ -KMT2D Western blot. Size marker (in kDa) is shown on the right.

**D:** Indicated histone H3 peptides (aa 1-8) were covalently coupled to Sulfolink-beads and incubated with bacterially expressed and purified GST-KMT2D PHD<sub>4-6</sub> mutant (4 mutations/amino acids exchanges in PHD<sub>6</sub>, which have been published to disrupt the KMT2D recognition of the H4 N-terminus (Dhar et al., 2012)) or wild type protein. Pulldown reactions and indicated input of GST-KMT2D proteins were resolved by SDS-PAGE and analyzed by  $\alpha$ -GST Western blot. Size marker (in kDa) is shown on the right.

**E:** Heatmap presents the KMT2D ChIP-seq profile (using the KMTD2 antibody from Santa Cruz) in NT2/D1 CT as well as KO cells  $\pm$  ATRA at the 4,583 enhancer-associated H3R2me2a binding sites (similar to Fig. 4A). These H3R2me2a sites of NT2/D1 CT cells are sorted according to their affiliation to the three clusters.

**F:** Boxplot analysis illustrates the normalized tag counts ( $\pm$  2kb centering H3R2me2a peaks) of KMT2D peaks (for samples of E). \*\*\*:  $p \leq 0.001$  using Welch's t-test.

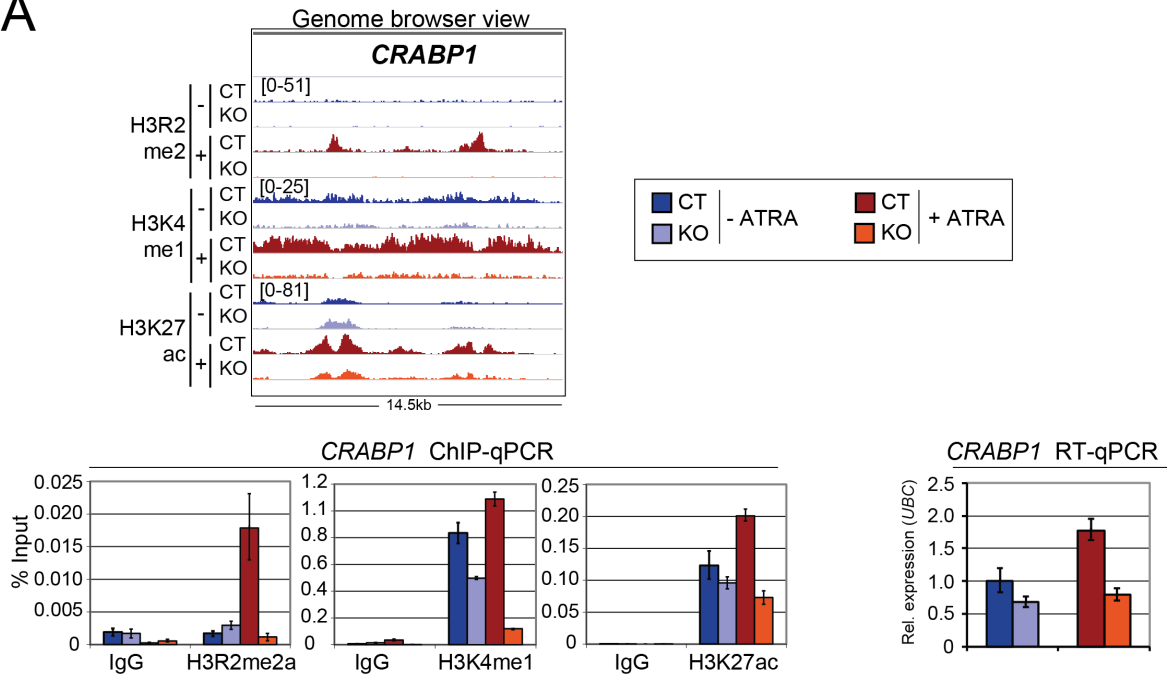
**G, H:** Fold change of H3R2me2a occupancy in NT2/D1 cells  $\pm$  ATRA was plotted versus fold change of KMT2D occupancy (detected using the KMTD2 antibody either from Abgent or from Santa Cruz) for all enhancer peaks (G) and for all promoter peaks (H). The Spearman correlation coefficient  $r$  and the  $p$ -val are indicated. A positive correlation between H3R2me2a and KMT2D occupancy was detectable for H3R2me2a enhancer peaks in G (but not promoter peaks in H).

**I:** Genome browser views of H3R2me2a and KMT2D ChIP-seq data sets, which were generated in NT2/D1 CT and KO cells  $\pm$  ATRA, are shown for the indicated gene loci. Positions of co-occurring H3R2me2a and KMT2D peaks, which reveal decreased occupancy upon PRMT6 deletion, are highlighted with black boxes above the top browser tracks. Data range is indicated in brackets.

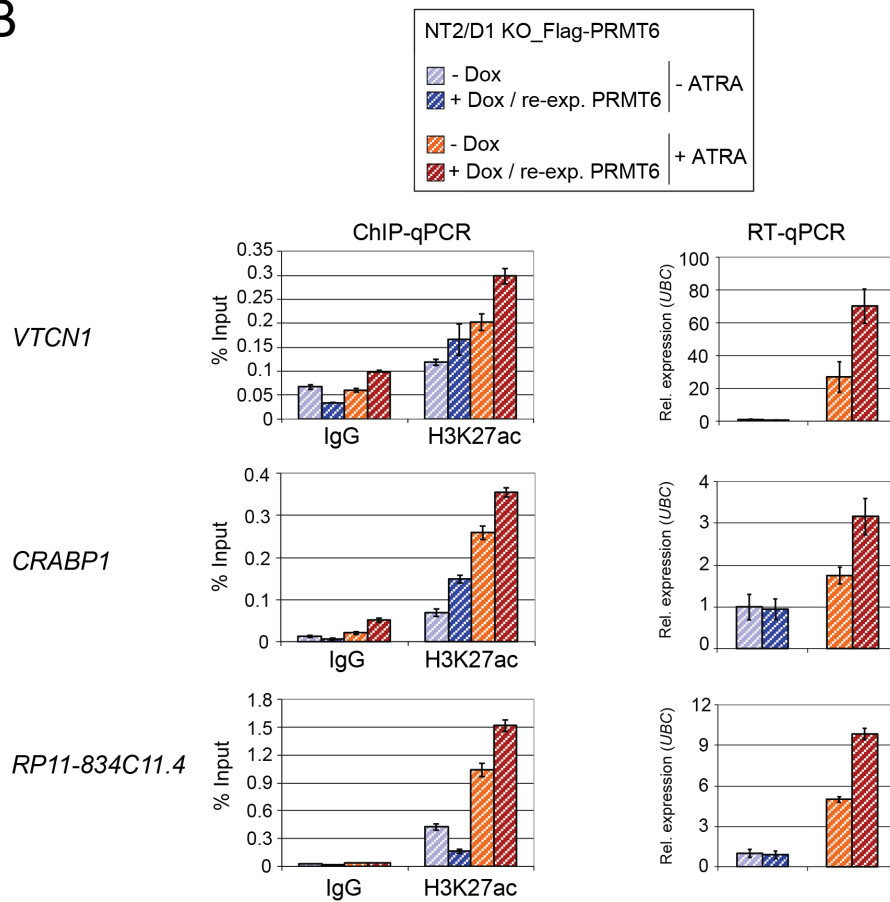


# Suppl.Figure S7

A



B



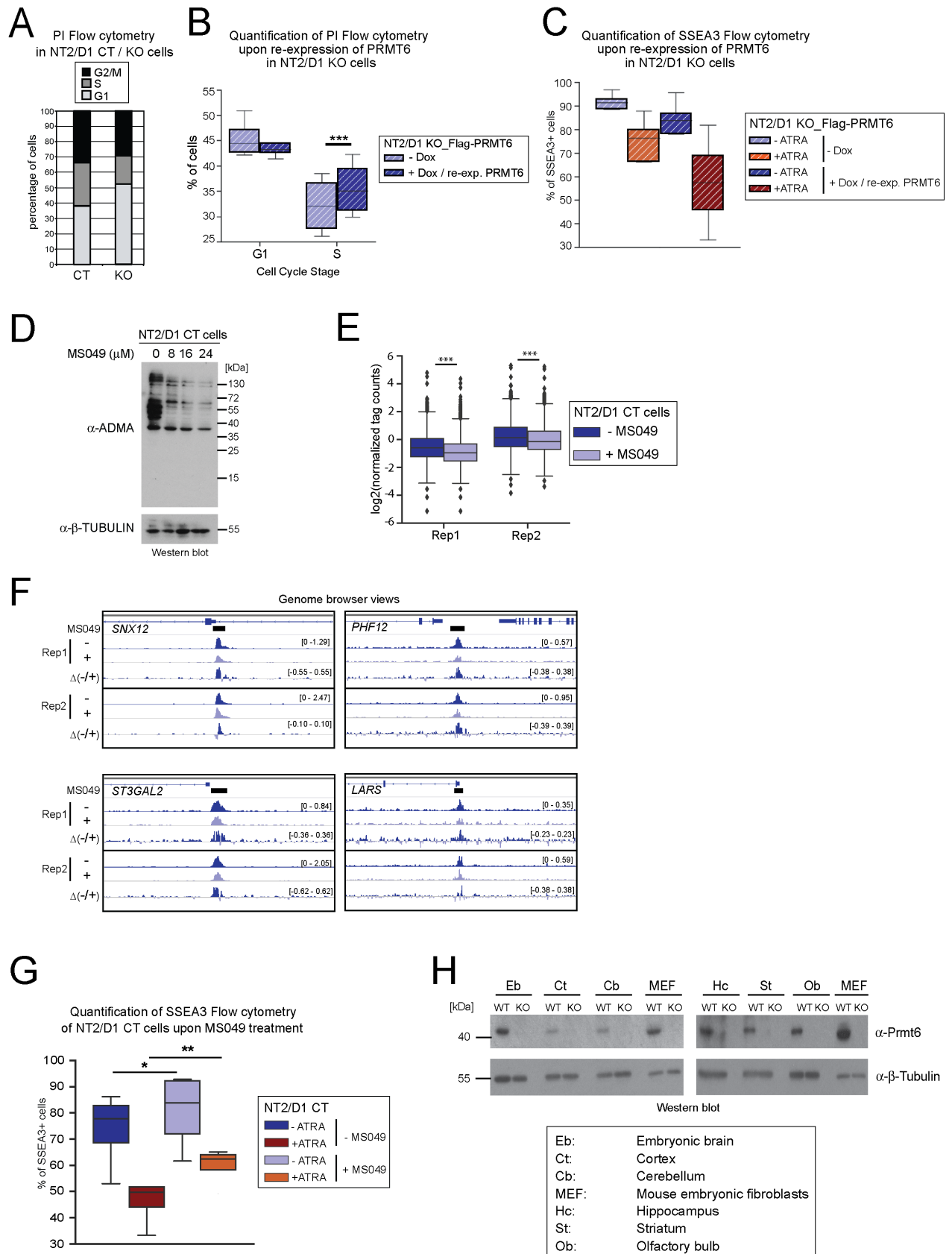
**Suppl.Figure S7**

**Validation of the cluster III gene *CRABP1* by ChIP-qPCR and RT-qPCR (A) and rescue of ATRA-induced H3K27ac deposition and transcriptional activation of target genes in NT2/D1 KO cells upon re-expression of Flag-PRMT6 (B). Related to Figure 5.**

**A:** Genome browser view of the *CRABP1* gene locus is shown for H3R2me2a, H3K4me1 and H3K27ac ChIP-seq data sets generated in NT2/D1 CT and KO cells -/+ ATRA (upper panel). Data range is indicated in brackets. ChIP-qPCR assays were performed in NT2/D1 cells using the indicated antibodies and primers encompassing the histone modification peaks. Recruitment is displayed in % input of chromatin, mean  $\pm$  SD of triplicates (lower left panels). Transcript levels of *CRABP1* was analyzed by RT-qPCR in NT2/D1 CT and KO cells -/+ ATRA. Values were normalized to *UBIQUITIN (UBC)* expression and presented relative to NT2/D1 CT cells - ATRA, mean  $\pm$  SD of triplicates (lower right panel).

**B:** ChIP-qPCR assays were performed in NT2/D1 KO cells in the absence (- doxycycline) or presence (+ doxycycline) of PRMT6 re-expression and in -/+ ATRA conditions using control antibodies (IgG),  $\alpha$ -H3K27ac and primers encompassing the H3K27ac peaks of the three indicated gene loci (corresponding genome browser views are depicted in A and Fig. 5A). Recruitment is displayed in % input of chromatin, mean  $\pm$  SD of triplicates (left panels). Total RNA was analyzed by RT-qPCR for transcript levels of *VTCN1*, *CRABP1* and *RP11-834C11.4*. Values were normalized to *UBIQUITIN (UBC)* expression and presented relative to the -Dox/-ATRA condition, mean  $\pm$  SD of triplicates (right panels).

# Suppl.Figure S8



### Suppl.Figure S8

#### Effect of PRMT6 on the cell cycle distribution and pluripotency/neural differentiation of NT2/D1 cells. Related to Figure 6.

**A:** Cell cycle distribution of NT2/D1 CT and KO cells was analyzed by flow cytometry using propidium iodide (PI) DNA staining.

**B:** NT2/D1 KO\_Flag-PRMT6 cells were cultured in the absence or presence of PRMT6 re-expression (-/+ doxycycline for 6 days). Cell cycle distribution was analyzed by flow cytometry using propidium iodide (PI) DNA staining. The quantification of four independent experiments is displayed. \*\*\*:  $p \leq 0.001$  using paired t-test.

**C:** NT2/D1 KO\_Flag-PRMT6 cells were cultured in the absence or presence of PRMT6 re-expression (-/+ doxycycline for 6 days) and +/- ATRA (last 3 days). The fraction of SSEA3-positive (SSEA3+) cells was measured by flow cytometry. The quantification of four independent experiments is displayed.

**D:** NT2/D1 CT cells were either untreated (0) or treated with the indicated concentrations of MS049 for 3 days. Subsequently, protein extracts were analyzed by Western blot using the indicated antibodies ( $\alpha$ -ADMA,  $\alpha$ -CDK2). CDK2 staining served as loading control. Size markers (in kDa) are shown on the right.

**E:** Boxplot analysis illustrates the normalized H3R2me2a tag counts of two ChIP-seq replicates in NT2/D1 CT cells +/- of 16  $\mu$ M MS049 for 3 days. \*\*\*:  $p \leq 0.001$  using Welch's t-test.

**F:** Genome browser views of the H3R2me2a ChIP-seq data sets of NT2/D1 CT cells +/- 16  $\mu$ M MS049 (replicates 1 and 2 of E) are depicted for four gene loci. H3R2me2a signal differences between +/- MS049 ( $\Delta$  +/-) are illustrated in a separate track for each replicate. Positions of H3R2me2a peaks, which show a decreased H3R2me2a occupancy upon MS049 treatment, are highlighted with black boxes above the top browser tracks. Normalized data range is indicated in brackets.

**G:** The fraction of SSEA3-positive (SSEA3+) NT2/D1 CT cells either untreated or treated for 3 days with ATRA, MS049 (16  $\mu$ M) or both was measured by flow cytometry. The quantification of four independent experiments is displayed. \*:  $p \leq 0.05$ ; \*\*:  $p \leq 0.01$  using paired t-test.

**H:** Brain tissue was dissected from *Prmt6* WT and KO mice (either E12.5 cortices pooled from several embryos or the indicated brain areas of adult animals, 16-20 weeks of age), immediately frozen in liquid nitrogen and stored at -80°C. Brain extracts were prepared by homogenizing frozen tissue in ice-cold lysis buffer (50mM Tris/HCl pH 7.4, 150mM NaCl, 0.5% NP-40, 0.1% SDS, plus protease-inhibitors). Furthermore, total protein lysates of MEF cell lines *Prmt6* WT and KO were employed. Protein extracts (20 $\mu$ g per sample) were analyzed by Western blot using  $\alpha$ -PRMT6.  $\beta$ -Tubulin staining served as loading control. Size markers (in kDa) are shown on the left.



## Supplemental Experimental Procedures

### Antibodies

The following antibodies were used: rabbit anti-GST-PRMT6 was produced using His-tagged proteins corresponding to amino acids 60–375 of human PRMT6, rabbit anti-PRMT6 (A300-929A, Bethyl Laboratories), mouse anti- $\beta$ -TUBULIN (MAB3408, Merck Millipore), anti-human CDK2 (sc-163, Santa Cruz Biotechnology), rabbit anti-asymmetrically dimethylated arginine (ADMA, 13522, Cell Signaling), rabbit anti-H3K4me3 (07-473, Merck Millipore), rabbit anti-H3K4me1 (39297, Active Motif), rabbit anti-H3K27ac (39133, Active Motif), rabbit anti-H3K27me3 (07-449, Millipore), rabbit anti-KMT2D (AP6183a, Abgent), rabbit anti-KMT2D (sc-293217, Santa Cruz), mouse anti-GST (sc-138, Santa Cruz Biotechnology), mouse anti-Flag (F3165, Sigma), rat anti-human SSEA3 DyLight 488 (MC-631, Life Technologies), rabbit anti-Pax6 (AB2237, Millipore), rabbit anti-Ki67 (Abcam, ab15580), goat anti-rabbit IgG (H+L) Alexa Fluor 488 (A11034, Life Technologies), and rat IgG (I4131, Sigma) and rabbit IgG (I5006, Sigma).

For the generation of anti-H3R2me2a antibodies, a peptide encompassing aa 2-9 of histone H3 with an asymmetrically dimethylated arginine (AR(me2)TKQTAR) was coupled to ovalbumin for immunization. Lou/c rats were immunized subcutaneously (s.c.) and intraperitoneally (i.p.) with a mixture of 40 $\mu$ g peptide, 5nmol CpG (TIB Molbiol) and an equal volume of incomplete Freund's adjuvant (Sigma). After 6 weeks, a boost without adjuvant was given i.p. and s.c. 3 days before fusion. Fusion of the myeloma cell line P3X63-Ag8.653 with the immune splenic cells was performed according to the standard procedure described by Koehler and Milstein (Köhler and Milstein, 1975). Hybridoma supernatants were screened in an enzyme-linked immunoassay on biotinylated dimethylated and unmethylated peptides. Supernatants positively tested on dimethylated peptides were further validated by dot plot analysis using H3 peptides (aa 2-9) either unmodified, monomethylated, asymmetrically dimethylated or symmetrically dimethylated at R2. The hybridoma cells of H3R2-reactive supernatants were cloned twice by limiting dilution.

### Plasmids and cloning

The following plasmids were used: pLentiCRISPRv1 (Addgene), pInducer20 (Meerbrey et al., 2011), pGEX-KMT2D PHD<sub>4-6</sub> wild type and mutant (E1516A/E1517A/D1518A/E1544A in PHD<sub>6</sub>) as well as pCMV2-Flag-MLL4 PHD<sub>4-6</sub> C-terminal fusion (Dhar et al., 2012). For design of gRNA (guide RNA), a web-based tool (<http://crispr.mit.edu>) was employed and the following target sites in human *PRMT6* or GFP (as control) were chosen:

gPRMT6.2 (plus strand):	5'-CCGTGCCGCGCTACGCCCCGC-3'
gPRMT6.8 (minus strand):	5'-TTTCTTGGGCTGCGACATCT-3'
gPRMT6.11 (plus strand):	5'-CTCGGACGTTTCGGTCCACG-3'
gPRMT6.12 (plus strand):	5'-CGCACCGATGCCTACCGCCT-3'
gPRMT6.14 (minus strand):	5'-GGTAGGCATCGGTGCGGACG-3'
gPRMT6.15 (plus strand):	5'-GACGGTACTGGACGTGGGCG-3'
Control_gRNA (GFP):	5'-GGAGCGCACCATCTTCTTCA-3'

Pairs of oligo nucleotides for these targeting sites (including the PAM sequence) were annealed and cloned into BsmBI-restricted plentiCRISPRv1 plasmid, which allows bicistronic expression of Cas9 nuclease and gRNA (Shalem et al., 2014).

Human full-length, wild type PRMT6 cDNA with N-terminal 3xFlag-tag (Flag-PRMT6) was amplified by PCR, cloned into the Acc65I and XhoI sites of pENTR4 entry vector and then transferred into pInducer20 via LR recombination (Gateway Cloning System, Invitrogen).

### Production of lentiviral particles and infection of NT2/D1 and U2OS cells

For CRISPR/Cas9-mediated deletion of *PRMT6* in NT2/D1 and U2OS cells and for the overexpression of Flag-PRMT6 (wild type) in NT2/D1 PRMT6 KO cells, HEK293T cells were transfected with the two packaging plasmids pMD2.G and psPAX2 together with the lentiviral expression plasmids encoding either the gRNA/controls and Cas9 (lentiCRISPRv1) or 3xFlag-PRMT6/empty vector (pInducer20). Transfections were performed using XtremeGENE (Roche). Supernatants containing lentiviral particles were harvested one and two days after transfection and concentrated using PEG. For CRISPR/Cas9 infections,  $1.6 \times 10^5$  cells were seeded in a 6-well plate. The next day, cells were infected in the presence of polybrene (8 $\mu$ g/ml) with viruses encoding either the combination of three *PRMT6* gRNAs (gP6\_2, gP6\_11 and gP6\_14 for KO-1; gP6\_8, gP6\_12 and gP6\_15 for KO-2) or the GFP control gRNA (for CT). Cell pools were selected using 1 $\mu$ g/ml puromycin and subjected to serial dilution to generate cell clones. For doxycycline-inducible expression of PRMT6, NT2/D1 KO cells were infected in the presence of polybrene (8 $\mu$ g/ml) with viruses containing either 3xFlag-PRMT6 or the corresponding empty vector. Cell pools

were selected using 800µg/ml G418. To induce PRMT6 expression, cells were treated for 6 days with 1µg/ml doxycycline (D9891, Sigma).

### Synthetic histone peptides, dot blot analysis and peptide pulldown

The following unmodified and modified N-terminal histone H3 and H4 peptides were used:

Name	Length (aa – aa)	C-terminus	Source
H3R2me0	1-8	Cystein	Peptide Specialty Laboratories
H3R2me1	1-8	Cystein	Peptide Specialty Laboratories
H3R2me2a	1-8	Cystein	Peptide Specialty Laboratories
H3R2me2s	1-8	Cystein	Peptide Specialty Laboratories
H3R2me0	1-30	Cystein	Peptide Specialty Laboratories
H3R2me1	1-30	Cystein	Peptide Specialty Laboratories
H3R2me2a	1-30	Cystein	Peptide Specialty Laboratories
H3R17me0	1-24	Biotin/Cystein	Peptide Specialty Laboratories
H3R17me2a	1-24	Biotin/Cystein	Peptide Specialty Laboratories
H3K4me3	1-15	Cystein	Peptide Specialty Laboratories
H3K9me1	1-15	Cystein	Peptide Specialty Laboratories
H3K9me2	1-15	Cystein	Peptide Specialty Laboratories
H3K9me3	1-15	Cystein	Peptide Specialty Laboratories
H3K27me2	1-30	Cystein	Peptide Specialty Laboratories
H4R3me0	1-15	Biotin/Cystein	Peptide Specialty Laboratories
H4R3me2a	1-15	Biotin/Cystein	Peptide Specialty Laboratories
H3R2me2a	1-15	Biotin	Hyllus et al., 2007
H3K4me3	1-15	Biotin	Hyllus et al., 2007
H3R2me2a/K4me3	1-15	Biotin	Hyllus et al., 2007

To monitor the quality and amount of synthesized peptides, 1µg of each was separated by SDS-PAGE and subjected to silver staining as previously described (Chevallet et al., 2006). For dot blot analysis, 1µg of each peptide was spotted onto nitrocellulose membrane, blocked with TBS/0.2% Tween 20/4%BSA for 1 h and stained with rat monoclonal α-H3R2me2a.

For peptide pulldowns, peptides were coupled to SulfoLink resin (Pierce) according to the manufacturer's protocol. Coupled peptides (10µg) were incubated under rotation for 2 h at 4°C with 1µg recombinant GST alone, GST-KMT2D PHD<sub>4-6</sub> (aa 1358-1572) wild type or mutant, which beforehand were expressed in *E. coli* BL21 and purified according to standard procedures. After extensive washes in BC Buffer (20mM HEPES pH 7.9, 150mM NaCl, 0.5% NP40, 20% glycerol, 0.4mM EDTA), bound proteins were analyzed by SDS-PAGE and immunoblotting. Alternatively, peptide pulldowns were performed using HeLa cell extracts overexpressing Flag-MLL4 PHD<sub>4-6</sub> C-terminal fusion protein. Therefore, HeLa cells were transfected using Fugene HD (Promega) according to the manufacturer's protocol. Coupled peptides (10µg) were blocked under rotation with PBS/2% BSA for 30 min and subsequently incubated with 2mg HeLa cell extract under rotation at 4°C for 2 h. After extensive washes in Flag-washing puffer (20mM HEPES pH 7.9, 150mM KCl, 20% glycerol, 0.1% Triton X-100, 0.2mM EDTA), bound proteins were analyzed by SDS-PAGE and immunoblotting.

### Protein isolation and Western Blot

For lysis, cells were resuspended in FT buffer (20mM Tris pH 7.8, 600mM KCl, 20% (v/v) glycerol, 10µg/ml protease inhibitors) and three times frozen and thawed. Cell extracts were subjected to benzonase treatment (0.25U/µl in presence of 7.5mM MgCl<sub>2</sub> for 1 h at 4°C). After centrifugation, cell lysates were analyzed by SDS-PAGE followed by immunoblotting.

### Flow cytometry

For quantification of the cell cycle distribution by flow cytometry, NT2/D1 cells were harvested, washed in ice-cold PBS and fixed in 80% ethanol for 10 min at -20°C. After complete permeabilization, cells were washed again and DNA was stained with 54µM propidium iodide (PI) in the presence of 38mM sodium citrate and 250µg/ml RNase A for 30 min at 37°C. Samples were then analyzed with a Becton Dickinson FACS Calibur. For pluripotency marker

(SSEA3) analysis by flow cytometry, NT2/D1 as well as HeLa cells ( $10^6$  each) were resuspended in PBS/0.5% BSA and stained with DyLight 488-conjugated anti-human SSEA3 at 4°C for 1 h in the dark. After washing (once in PBS, twice in PBS/0.5% BSA) cells were resuspended in PBS and measured with a Becton Dickinson FACS Calibur. Data were analyzed with FlowJo version 7.6.5 (Tree Star) using HeLa cell fluorescence as a negative control.

## Animals

Constitutive *Prmt6*  $-/-$  (KO) mice were provided by the laboratory of Stephane Richards (Neault et al., 2012). For generation of *Prmt6*  $-/-$  (KO),  $+/-$  (HET) and  $+/+$  (WT) embryos of embryonic day 12.5 (E12.5), pregnant female mice (*Prmt6* HET) were sacrificed by cervical dislocation and embryos were decapitated. Embryo heads were fixed for 3 h in 4% PFA at 4°C, then transferred into PBS. For cryoprotection embryo heads were incubated for 2 days in 15% sucrose/PBS followed by incubation for 2 days in 30% sucrose/PBS before freezing on dry ice and storage at  $-80^{\circ}\text{C}$ . For immunofluorescence (IF) staining, embryo heads were cut into 20  $\mu\text{m}$ -thick coronal sections using Leica microtome CM3050S. Sections were postfixed (10 min in 4% PFA), washed twice for 5 min each in 50mM glycine and in PBS before incubating for 60 min in blocking solution (2% BSA, 3% goat serum, 0.5% NP40 in PBS). Incubation with primary antibodies (anti-Pax6 1:200 and anti-Ki67 1:50) was performed overnight at 4°C in blocking solution without goat serum. Subsequently, sections were washed 3x with PBS, blocked for 30 min in blocking solution and then secondary antibodies were supplied for 2 h. Finally, the sections were counter-stained with 5  $\mu\text{g}/\text{ml}$  Propidium-Iodid (Sigma P4170) for 15 min, washed 3x with PBS and embedded in DABCO medium and stored at 4°C. Fluorescence images were acquired using confocal Leica TCS SP5 II microscope (20x Leica objective) and the software Leica LAS AF as well as Fiji. Neural progenitor cell numbers (Pax6- or Ki67-positive cells) were quantified from a standardized area (125 x 125  $\mu\text{m}$  at 50-fold magnification) of 5-6 embryos of each condition. The VZ layer width (Pax6-positive) as well as the VZ/SVZ layer width (Ki67-positive) was measured at three positions of four independent pictures of each embryo (5-6 embryos per condition) and the mean layer width was calculated.

## RNA isolation and reverse transcription quantitative PCR (RT-qPCR)

Total RNA was isolated using RNA-Mini-Kit (SeqLab, Göttingen, Germany). For cDNA synthesis 0.5-1  $\mu\text{g}$  of total RNA was used as template for random hexamer oligonucleotides and M-MLV reverse transcriptase (Thermo Scientific) according to the manufacturer's instruction. cDNA was subjected to PCR amplification using different primers (listed below) and Absolute qPCR SYBR Green Mix (Thermo Scientific).

Forward (fwd) and reverse (rev) primers used for RT-qPCR of indicated gene transcripts:

Name	Sequence (5'-3')
hARID1A RT fwd	CCAACAAAGGAGCCACCA
hARID1A RT rev	TTGCCCATCTGATCCATTG
hCNOT1 RT fwd	TGCAGCAGTATGATCTTCACCT
hCNOT1 RT rev	CATCCACCAGCAGGATTTTT
hCRABP1 RT fwd	TCAACTTCAAGGTCGGAGAAG
hCRABP1 RT rev	TCATTCTCCCAAGTGGCTAAA
hID1 RT fwd	CCAGAACCGCAAGGTGAG
hID1 RT rev	GGTCCCTGATGTAGTCGATGA
hLARS RT fwd	TGACAAATTTTCAGCAGATGGA
hLARS RT rev	GGCATCTTCTACAGTGTACCA
hMITF RT fwd	CAAAAGTCAACCGCTGAAGA
hMITF RT rev	AGGAGCTTATCGGAGGCTTG
hNANOG RT fwd	TCCAGCAGATGCAAGAATC
hNANOG RT rev	TTGCTATTCTTCGGCCAGTT
hOCT4 RT fwd	TGAAGAACAAGTGCCAAATAGC
hOCT4 RT rev	GCGGCTATACAAAGTGGACAA
hPSMF1 RT fwd	GTTACTTCGGCTTGGGTGTC
hPSMF1 RT rev	CATACAGGTCTTTATTGTTGTTCCA
hRP11-834C11.4 RT fwd	GGAAATCTAGATGAGCCTGTCC
hRP11-834C11.4 RT rev	CTGCTACCAAGGTCTGGA
hST3GAL2 RT fwd	GTCTGGACCCGAGAGAACAT
hST3GAL2 RT rev	TGGTGTGTGTGACTTGAAGT
hUBC RT fwd	CACTTGGTCCTGCGCTTGA

hUBC RT rev	CAATTGGGAATGCAACAACCTTTAT
hVTCN1 RT fwd	GCAGATCCTCTTCTGGAGCAT
hVTCN1 RT rev	CCAGCTGAGGCGACAGTAGT

For RNA sequencing (RNA-seq), total RNA was isolated from three biological replicates using RNA-Mini-Kit. RNA quality was assessed using the Experion RNA StdSens Analysis Kit (BioRad). RNA-seq libraries were prepared from total RNA using the TruSeq Stranded mRNA LT kit (Illumina) according to the manufacturer's instructions. Quality of sequencing libraries was controlled on a Bioanalyzer 2100 using the Agilent High Sensitivity DNA Kit (Agilent). Pooled sequencing libraries were quantified with digital PCR (QuantStudio 3D, Thermo Fisher) and sequenced on the HiSeq 1500 platform (Illumina) in Rapid-Run mode with 50 base single reads.

### Chromatin immunoprecipitation and quantitative PCR (ChIP-qPCR) and ChIP-seq

For immunoprecipitation of histone marks, cells were crosslinked for 10 min with 1% formaldehyde at room temperature. For immunoprecipitation of KMT2A and KMT2D, disuccinimidyl glutarate (DSG) was added at a final concentration of 2mM to the cells and incubated 45 min at room temperature. After 2 washings in PBS, cells were crosslinked with formaldehyde as described above. The reaction was stopped by addition of glycine at a final concentration of 0.125M for 5 min. For KMT2D ChIP, cells were lysed in Lysis buffer B (10mM HEPES/KOH pH6.5, 10mM EDTA, 0.5mM EGTA, 0.25% Triton X 100) for 10 min on ice, centrifuged and resuspended in Lysis buffer C (10mM HEPES/KOH pH6.5, 10mM EDTA, 0.5mM EGTA, 200mM NaCl). After a 20 min incubation on ice and centrifugation, Lysis buffer D (50mM Tris/HCl pH 8.5, 10mM EDTA, 1% SDS, protease inhibitors) was added to the cells and incubated for 20 min on ice. Nucleic lysates were sonified using the Bioruptor (Diagenode) for 2 times 7 min (30 sec ON, 30 sec OFF; HIGH amplitude). After centrifugation, 100µg chromatin was subjected to the OneDay ChIP Kit (Diagenode) according to the manufacturer's instructions. For the other factors and for histone modifications, cell lysis was performed in Lysis buffer I (5mM PIPES pH 8, 85mM KCl, 0.5% NP-40, protease inhibitors) for 10 min on ice. After centrifugation, cell pellets were resuspended in Lysis buffer II (10mM Tris/HCl pH 7.5, 150mM NaCl, 1% NP-40, 1% sodium deoxycholate, 0.4% SDS, 1mM EDTA, protease inhibitors) and incubated on ice for 20 min. Chromatin was fragmented at 4°C by sonification using a Branson Sonifier W-250-D (80x 1 sec, 3 sec pause, 15% amplitude). Subsequently, 100µg chromatin were precleared with blocked Protein A or Protein G Sepharose (1mg/ml BSA and 400µg/ml salmon sperm DNA in Lysis buffer II) for 2 h at 4°C. For immunoprecipitations except H3R2me2a, 4µg of antibodies were added to the precleared chromatin and incubated overnight at 4°C. To immobilize immunoprecipitates, 60µl of Protein A Sepharose were added for 2 h at 4°C and subjected to successive washing steps. For anti-H3R2me2a immunoprecipitations, 1-2ml hybridoma supernatant was incubated with blocked Protein G beads for 2 h at 4°C. After washes in Lysis buffer II, antibodies-precoupled beads were added to 100µg of precleared chromatin and incubated overnight at 4°C. The next day, immobilized immunoprecipitates were washed twice with washing buffer I (20mM Tris/HCl pH 8.1, 150mM NaCl, 2mM EDTA, 0.1%SDS, 1%Triton X-100), washing buffer II (20mM Tris/HCl pH 8.1, 500mM NaCl, 2mM EDTA, 0.1% SDS, 1% Triton X-100), washing buffer III (10mM Tris/HCl pH 8.1, 250mM LiCl, 1mM EDTA, 0.1% sodium deoxycholate, 1% NP-40) and TE buffer. Chromatin was eluted twice with 250µl 0.1M NaHCO<sub>3</sub> and 1% SDS for 15 min at RT. Crosslinking was reversed by incubation with 1µl of 10mg/ml Proteinase K and RNase A for 3 h at 55°C followed by overnight at 65°C. DNA was purified *via* QIAquick columns (QIAGEN) and either processed for ChIP-seq or analyzed by ChIP-qPCR using different primers (listed below) and Absolute qPCR SYBR Green Mix (Thermo Scientific). For ChIP-seq, libraries were prepared according to the manufacturer's protocol (Diagenode, MicroPlex Library Preparation Kit).

Forward (fwd) and reverse (rev) primers used for ChIP-qPCR of indicated genomic loci, either amplifying the specific PRMT6 binding site (=spec) or a corresponding control region (=ctr):

Name	Sequence (5'-3')
ARID1A ChIP spec fwd	GTGAGGGAGAGCTAGCGAGA
ARID1A ChIP spec rev	GCGCAGATTGGAGAACTAGG
ATG4C ChIP spec fwd	TTGGGTTGGCTCTATCTTGG
ATG4C ChIP spec rev	TCCTCTCGAGCACTTGGACT
ATG4C ChIP CT fwd	GGCAAAACCCCATCTCTACA
ATG4C ChIP CT rev	TTGATCTCCCAGGCTCAAGT
C12orf57 ChIP spec fwd	TTTTGGTGGTCTTGATGCAG
C12orf57 ChIP spec rev	GTTCAGCGGAGGTAAATGGA

CLEC16A ChIP spec fwd	TAGTCCGTTTCGCGGAGTC
CLEC16A ChIP spec rev	CAGCCCAGCACTGACATTC
CNOT1 ChIP spec fwd	AAGCAAGCCAGGTTGTGACT
CNOT1 ChIP spec rev	GTGACTACAACCCCCAGCAT
CNOT1 ChIP ctr fwd	CCAGGCAATGACCAATTCTT
CNOT1 ChIP ctr rev	AATCAGTGCCCTTTTGATGG
CRABP1 ChIP spec fwd	TTGATCGGGAGAGAGAATGG
CRABP1 ChIP spec rev	CTGCAGGAGCCAGAGACAA
CRABP1 ChIP K4me1spec fwd	AGCAGCGACCAGACCAAG
CRABP1 ChIP K4me1spec rev	TTCACCCCACCTCACTTAG
FASTKD1 ChIP spec fwd	GAGACATGACCTTTCCCATGA
FASTKD1 ChIP spec rev	ACGTCCATTTCACCCACCT
FASTKD1 ChIP CT fwd	TTCCTGTCTGGTTTCCATTG
FASTKD1 ChIP CT rev	AAGGCAAATGTTAGGGAGGAA
ID1 ChIP spec fwd	CGCACTCTCATTCCACGTT
ID1 ChIP spec rev	TTCATGATTCTTGGCGACTG
KDM5A ChIP spec fwd	TCTTGCAAGGCTTTTCCACT
KDM5A ChIP spec rev	GAAGGAAAGGCCAGACACAC
KDM5A ChIP CT fwd	TTTTCGGTTTCCTGGTACATAAA
KDM5A ChIP CT rev	CAGAGCAAGACTCTGTCTCAAAAA
LARS ChIP spec fwd	GTCTACCCGATAGGCCCACT
LARS ChIP spec rev	GCACTGCATCATGGACTTTG
LARS ChIP ctr fwd	CAAGCCAATGTTCTGCTTCA
LARS ChIP ctr rev	CCAGTGGGGCATTATGAAAT
MITF ChIP spec fwd	AGCAAGTGGGGAGAGAGGA
MITF ChIP spec rev	GCTCCCACGAAAACCTACAGC
NUDCD1 ChIP spec fwd	TCGCACAGAGACTGGGAAG
NUDCD1 ChIP spec rev	CTACATAGCCCAGCATGCAA
NUDCD1 ChIP CT fwd	TTTGCAGAGTTCTCCCAAAAA
NUDCD1 ChIP CT rev	TCTTCTTCTCAACCCTTACAAAGA
OCT4 ChIP spec fwd	AAGAAGCCTGGGAGGGACT
OCT4 ChIP spec rev	GTTAGAGCTGCCCCCTCTG
PHF12 ChIP spec fwd	CAACGCCAAAGGGTCTAAAG
PHF12 ChIP spec rev	GACTCTTCCCCGGGTCTATC
PHF12 ChIP CT fwd	CCCAACAAAATCAAGAGAGCA
PHF12 ChIP CT rev	CTGAGGCAGGAGAATCAGTTG
PSMF1 ChIP spec fwd	ATGTGGACGGTAGCAAGCA
PSMF1 ChIP spec rev	CACCTTGCTGAGAGGCAGA
RP11-834C11.4 ChIP spec fwd	GGCCAGGATTAACCACAGAA
RP11-834C11.4 ChIP spec rev	ACACTGTCCAGAGCCCAGAC
RP11-834C11.4 ChIP K4me1spec fwd	GCAGAGGGATTGCTCAACAT
RP11-834C11.4 ChIP K4me1spec rev	TGGACTGTGAGGGACACAAA
SNX12 ChIP spec fwd	TCATAGGTGGTGAAGCGCG
SNX12 ChIP spec rev	CCGCCAAGTAACTTCCTGGA
ST3GAL2 ChIP spec fwd	GCATGCTGGGATATGGAGTC
ST3GAL2 ChIP spec rev	CGCTGTCTTCTGGGAGATGT
ST3GAL2 ChIP CT fwd	GAGTGCAGTGGTGCGATCT
ST3GAL2 ChIP CT rev	AAAATTAGCCAGGCATGGTG
VTCN1 ChIP spec fwd	GGAAGTAGGCCCCAAAAGAG
VTCN1 ChIP spec rev	CTGTCAGGCCATCCATCTG
VTCN1 ChIP K4me1spec fwd	TCCAGGGCACCAGTCTTAGT
VTCN1 ChIP K4me1spec rev	CCATCTCCAGGTCAGTGTCA

## Bioinformatic analysis

### ChIP-seq

Replicate samples were sequenced as single-end reads using an Illumina HiSeq 1500. Reads were de-multiplexed using Illumina bcl2fastq and aligned with Bowtie2 (Langmead and Salzberg, 2012) against *Homo sapiens*, release 74, Ensembl genome. After alignment de-duplication was performed to remove PCR duplicates. For visualization, de-duplicated BAM files were converted to TDF with parameter (window\_size = 10) using IGV tools and visualized using IGV 2.3.82 (Robinson et al., 2011) with option import as normalized tracks for some profiles mentioned in the corresponding legends. Peak calling was performed using MACS (Zhang et al., 2008). All peaks were called accounting the background with corresponding IgG control ChIP-seq data. Peaks were further filtered with criteria  $\geq 35$  tag counts and  $\geq 2$ -fold enrichment above IgG and density-based criteria (peak length/tag count  $\leq 15$ ). Heatmaps were created with custom script where read density data were extracted in 60 bins 100bp/bin from -3kb to +3kb by keeping the corresponding peak summit as centre. To further investigate the structure in data, k-means clustering (algorithm=auto, distance metric=euclidean, number of cluster=10, iterations=1000) in scikit-learn was employed. The read coverage was normalized by dividing with total read count, multiplying by one million and then plotted with R, heatmap3 package. In Fig. 3A and Fig. S5C normalization constant between CT and KO ChIP-seq was calculated by resampling all H3K4me3 peaks (assuming that the majority of H3K4me3 was not affected by PRMT6 loss) in a subset with replacement and this process was repeated for 10000 iteration. Normalization constant was calculated as the mean difference between CT and KO for 10000 iterations. In the boxplot analysis (Fig. 4B, Fig. S6F) tag densities for the H3K4me3, H3K4me1, H3K27ac and KMT2D samples were retrieved  $\pm 2$ Kb from the summit of H3R2me2a peaks and normalized. In Figure S6 (A, B, G and H), normalized tag densities for H3R2me2a, H3K4me1, H3K27ac and KMT2D in + ATRA and - ATRA conditions were divided to obtain the fold change of enrichment. These fold changes were used in calculating the Spearman correlation coefficient between two histone modifications.

### RNA-seq

Samples were prepared as biological triplicates and sequenced as single-end reads using an Illumina HiSeq 1500. Reads were aligned with Tophat2 (Kim et al., 2013) against *Homo sapiens*, release 74, Ensembl genome. Read coverage (number of overlapping reads per base pair) was calculated over non-overlapping exons. The exon counts were aggregated for each gene to build a read count table using SubRead function featureCount (Liao et al., 2013). Differentially regulated genes were calculated using DESeq2 (Love et al., 2014). For differentially regulated genes a threshold ( $FC \geq 2$  or  $FC \leq -2$ , adj-pval  $\leq 0.01$ ) was followed. To analyze the biological significance of genes, Metascape (<http://metascape.org>) (Tripathi et al., 2015) was used for gene ontology analysis. We normalized expression data with transcript per million (TPM) (Wagner et al., 2012) for quantile based binning of genes expression. For significance testing of differences between two sample distributions Welch's t-test was employed.

### External Datasets

SRR1204514: H3K4me3 U2OS

SRR2558762: H3K4me1 U2OS

SRR1204515: H3K27ac U2OS



## Supplemental References

- Chevallet, M., Luche, S., and Rabilloud, T. (2006). Silver staining of proteins in polyacrylamide gels. *Nat. Protoc.* *1*, 1852–1858.
- Dhar, S.S., Lee, S.H., Kan, P.Y., Voigt, P., Ma, L., Shi, X., Reinberg, D., and Lee, M.G. (2012). Trans-tail regulation of MLL4-catalyzed H3K4 methylation by H4R3 symmetric dimethylation is mediated by a tandem PHD of MLL4. *Genes Dev.* *26*, 2749–2762.
- Hyllus, D., Stein, C., Schnabel, K., Schiltz, E., Imhof, A., Dou, Y., Hsieh, J., and Bauer, U.-M. (2007). PRMT6-mediated methylation of R2 in histone H3 antagonizes H3 K4 trimethylation. *Genes Dev.* *21*, 3369–3380.
- Kim, D., Pertea, G., Trapnell, C., Pimentel, H., Kelley, R., and Salzberg, S.L. (2013). TopHat2: accurate alignment of transcriptomes in the presence of insertions, deletions and gene fusions. *Genome Biol.* *14*, R36.
- Köhler, G., and Milstein, C. (1975). Continuous cultures of fused cells secreting antibody of predefined specificity. *Nature* *256*, 495–497.
- Langmead, B., and Salzberg, S.L. (2012). Fast gapped-read alignment with Bowtie 2. *Nat. Methods* *9*, 357–359.
- Liao, Y., Smyth, G.K., and Shi, W. (2013). The Subread aligner: Fast, accurate and scalable read mapping by seed-and-vote. *Nucleic Acids Res.* *41*.
- Love, M.I., Huber, W., and Anders, S. (2014). Moderated estimation of fold change and dispersion for RNA-seq data with DESeq2. *Genome Biol.* *15*, 550.
- Meerbrey, K.L., Hu, G., Kessler, J.D., Roarty, K., Li, M.Z., Fang, J.E., Herschkowitz, J.I., Burrows, A.E., Ciccio, A., Sun, T., et al. (2011). The pINDUCER lentiviral toolkit for inducible RNA interference in vitro and in vivo. *Proc. Natl. Acad. Sci.* *108*, 3665–3670.
- Robinson, J.T., Thorvaldsdóttir, H., Winckler, W., Guttman, M., Lander, E.S., Getz, G., and Mesirov, J.P. (2011). Integrative Genome Viewer. *Nat. Biotechnol.* *29*, 24–26.
- Shalem, O., Sanjana, N.E., Hartenian, E., Shi, X., Scott, D.A., Mikkelsen, T.S., Heckl, D., Ebert, B.L., Root, D.E., Doench, J.G., et al. (2014). Genome-Scale CRISPR-Cas9 Knockout Screening in Human Cells. *Science* (80- ). *343*, 84–87.
- Tripathi, S., Pohl, M.O., Zhou, Y., Rodriguez-Frandsen, A., Wang, G., Stein, D.A., Moulton, H.M., Dejesus, P., Che, J., Mulder, L.C.F., et al. (2015). Meta- and Orthogonal Integration of Influenza “oMICs” Data Defines a Role for UBR4 in Virus Budding. *Cell Host Microbe* *18*, 723–735.
- Umlauf, D., Goto, Y., Delaval, K., Wagschal, A., Arnaud, P., and Feil, R. Chromatin immunoprecipitation on native chromatin from cells and tissues (PROT22). 2005. Epigenome Network of Excellence. [www.epigenome-noe.net](http://www.epigenome-noe.net)
- Wagner, G.P., Kin, K., and Lynch, V.J. (2012). Measurement of mRNA abundance using RNA-seq data: RPKM measure is inconsistent among samples. *Theory Biosci.* *131*, 281–285.
- Zhang, Y., Liu, T., Meyer, C.A., Eeckhoutte, J., Johnson, D.S., Bernstein, B.E., Nussbaum, C., Myers, R.M., Brown, M., Li, W., et al. (2008). Model-based Analysis of ChIP-Seq (MACS). *Genome Biol.* *9*, R137.